Monthly Notices
of the
ROYAL ASTRONOMICAL SOCIETY

MNRAS **459,** 257–276 (2016)
Advance Access publication 2016 March 20

doi:10.1093/mnras/stw667

AGN are cooler than you think: the intrinsic far-IR emission from QSOs

M. Symeonidis,[1,2]★ B. M. Giblin,[2,3] M. J. Page,[1] C. Pearson,[4] G. Bendo,[5] N. Seymour[6] and S. J. Oliver[2]

[1]*Mullard Space Science Laboratory, University College London, Holmbury St. Mary, Dorking, Surrey RH5 6NT, UK*
[2]*Astronomy Centre, Department of Physics & Astronomy, University of Sussex, Brighton BN1 9QH, UK*
[3]*University of Birmingham, Edgbaston, Birmingham, West Midlands B15 2TT, UK*
[4]*RAL Space, Rutherford Appleton Laboratory, Chilton, Didcot, Oxfordshire OX11 0QX, UK*
[5]*UK ALMA Regional Centre Node, Jodrell Bank Centre for Astrophysics, Alan Turing Building, School of Physics and Astronomy, The University of Manchester, Oxford Road, Manchester M13 9PL, UK*
[6]*Department of Physics and Astronomy, Curtin University, Kent Street, Bentley, Perth, WA 6102, Australia*

Accepted 2016 March 16. Received 2016 March 16; in original form 2015 August 9

ABSTRACT

We present an *intrinsic* AGN spectral energy distribution (SED) extending from the optical to the submm, derived with a sample of unobscured, optically luminous ($\nu L_{\nu,5100} > 10^{43.5}$ erg s^{-1}) QSOs at $z < 0.18$ from the Palomar Green survey. The intrinsic AGN SED was computed by removing the contribution from stars using the 11.3 μm polycyclic aromatic hydrocarbon (PAH) feature in the QSOs' mid-IR spectra; the 1σ uncertainty on the SED ranges between 12 and 45 per cent as a function of wavelength and is a combination of PAH flux measurement errors and the uncertainties related to the conversion between PAH luminosity and star-forming luminosity. Longwards of 20 μm, the shape of the intrinsic AGN SED is independent of the AGN power indicating that our template should be applicable to all systems hosting luminous AGN ($\nu L_{\nu,5100}$ or $L_{\rm X(2-10\,keV)} \gtrsim 10^{43.5}$ erg s^{-1}). We note that for our sample of luminous QSOs, the average AGN emission is at least as high as, and mostly higher than, the total stellar powered emission at all wavelengths from the optical to the submm. This implies that in many galaxies hosting powerful AGN, there is no 'safe' broad-band photometric observation (at $\lambda < 1000$ μm) which can be used in calculating star formation rates without subtracting the AGN contribution. Roughly, the AGN contribution may be ignored only if the intrinsic AGN luminosity at 5100 AA is at least a factor of 4 smaller than the total infrared luminosity ($L_{\rm IR}$, 8–1000 μm) of the galaxy. Finally, we examine the implication of our work in statistical studies of star formation in AGN host galaxies.

Key words: galaxies: active – galaxies: general – quasars: general – infrared: galaxies.

1 INTRODUCTION

The debate about a possible connection between galaxies and their supermassive black holes has been long-standing, originally fuelled by two global observations: (i) the correlation between black hole mass and bulge stellar mass or velocity dispersion in the nearby Universe (e.g. Magorrian et al. 1998; Ferrarese & Merritt 2000) and (ii) the comparable temporal evolution of the star formation rate (SFR) density and AGN accretion rate density (e.g. Boyle & Terlevich 1998). The idea that star formation and AGN accretion are causally connected has become an essential component in theoretical models of galaxy evolution, as AGN feedback is required to regulate the formation and number of massive galaxies (e.g. Bower et al. 2006; Croton et al. 2006).

The connection between AGN and their hosts has often been examined by means of the location of galaxies in colour–magnitude space (e.g. Strateva et al. 2001; Baldry et al. 2004). The sparsity of galaxies in transition between the 'blue cloud' of star-forming galaxies and the 'red sequence' of passive ellipticals has founded hypotheses in which energetic events associated with the central black hole are responsible for terminating star formation on short time-scales (e.g. Granato et al. 2004; Springel, Di Matteo & Hernquist 2005). Studies have examined, albeit inconclusively, whether the colours of AGN hosts are an indication of the quenching of star formation; Georgakakis et al. (2008) and Schawinski et al. (2009) find that AGN host galaxies are transitioning from the blue cloud to the red sequence, supporting such a scenario, whereas Westoby, Mundell & Baldry (2007) and Cardamone et al. (2010) find a large fraction of AGN in passive galaxies. Recently, Symeonidis et al. (2013b) found that the overlap in optical

★ E-mail: m.symeonidis@ucl.ac.uk

colour–colour and colour–magnitude space of SFGs and type II AGN at $z < 1.5$ indicates that SFGs are on average three times more likely to host a type II AGN than would be expected serendipitously, if AGN and star formation events were unrelated.

Although measured SFRs of AGN host galaxies span a large range, sometimes reaching a few thousand $M_{\odot}$ yr^{-1} (e.g. Isaak et al. 2002; Priddey et al. 2003a,b; Lutz et al. 2008; Silverman et al. 2009; Mainieri et al. 2011; Dai et al. 2012; Khan-Ali et al. 2015; Podigachoski et al. 2015), it is not yet clear whether and/or how the AGN accretion rate and its host's SFR are connected. Some studies show that the AGN accretion rate is well correlated with SFR over a large range in AGN luminosity (e.g. Rovilos et al. 2012; Chen et al. 2013; Hickox et al. 2014), whereas others report that the correlation is almost non-existent at low AGN luminosities but becomes stronger at high AGN luminosities (e.g. Shao et al. 2010; Rosario et al. 2012, 2013), or that the two quantities are not correlated (e.g. Rawlings et al. 2013; Azadi et al. 2015; Stanley et al. 2015). Page et al. (2012) and Barger et al. (2015) show that the most luminous AGN do not reside in the most highly star-forming hosts, whereas Harrison et al. (2012) present contrasting results and Rafferty et al. (2011) find that luminous AGN are more common in systems with high SFRs.

A possible reason for discrepant results amongst these studies, could be the difficulties encountered when dealing with AGN contamination to the galaxies' spectral energy distributions (SEDs) and SFR estimates. Currently, one of the most widely used methods of calculating SFRs is with IR/submm continuum data, since IR emission is an excellent tracer of young SF/starburst regions, particularly in galaxies with high SFRs where the contribution from dust heating from older stars is minimal. However, in AGN host galaxies, in addition to starlight-heated dust emission, the infrared SED also includes a contribution from the AGN: UV/optical light from the AGN is expected to be intercepted by dust in its vicinity (i.e. the torus) as well as dust distributed over kpc scales in the host galaxy. Indeed, unless the torus is all enveloping and no light can escape, then a scenario whereby UV/optical light from the AGN is not intercepted by the dust over kpc scales in the host galaxy is not realistic. A similar argument was made by Sanders et al. (1989) who concluded that AGN must contribute to dust heating over kpc scales. As a result, when dealing with dust-reprocessed UV/optical radiation from an AGN, two components need to be taken into account: (i) IR emission from the AGN-heated dust in the torus and (ii) IR emission from AGN-heated dust in the host galaxy, the former peaking at shorter wavelengths than the latter. Here, we aim to provide an intrinsic AGN SED up to 1000 μm, reproducing as far as possible the total AGN contribution in the far-IR/submm. Our motivation is simple: if we are to truly understand the connection between AGN and star formation then we must be confident of the characteristics of the intrinsic AGN emission.

The paper is laid out as follows: in Section 2, we describe our criteria for the sample selection and finalize the sample for this work. In Section 3, we describe the fitting of SEDs and produce an intrinsic AGN template. In Section 4, we discuss our results and we conclude with Section 5. Throughout, we adopt a concordance cosmology of $H_0 = 70$ km s^{-1} Mpc^{-1}, $\Omega_{\rm M} = 1{-}\Omega_{\Lambda} = 0.3$.

2 THE SAMPLE

2.1 Selection criteria

As outlined in Section 1, our study aims to understand the intrinsic AGN SED, particularly in the infrared. Naturally, the ideal sample for this would be galaxies with no stars so that the total broad-band SED would be the result of AGN emission only (direct or reprocessed). This is of course impossible, so the next best approach is to select a sample of galaxies whose stellar output is small compared to the AGN emission. Low-luminosity AGN are not appropriate for such a study, as their radiative output is often drowned by their host's over most of the electromagnetic spectrum making their intrinsic SEDs difficult to extract. Our first requirement is, therefore, that our sample should be composed of optically luminous, broad-line AGN which dominate the global SED, at least from X-ray to near-IR wavelengths. The second requirement is that the sample is at low redshift where on average SFRs are low, but also so that available photometry can probe longer rest-frame wavelengths. Since our aim is to extract the AGN SED from the galaxies' total emission, the third requirement is that we have a measure of the SFR independently of the galaxies' broad-band SED. For optically luminous AGN, the optical spectra cannot be used to extract information about the host, whereas the mid-IR spectra, and in particular polycyclic aromatic hydrocarbon (PAH) features, are a viable alternative.

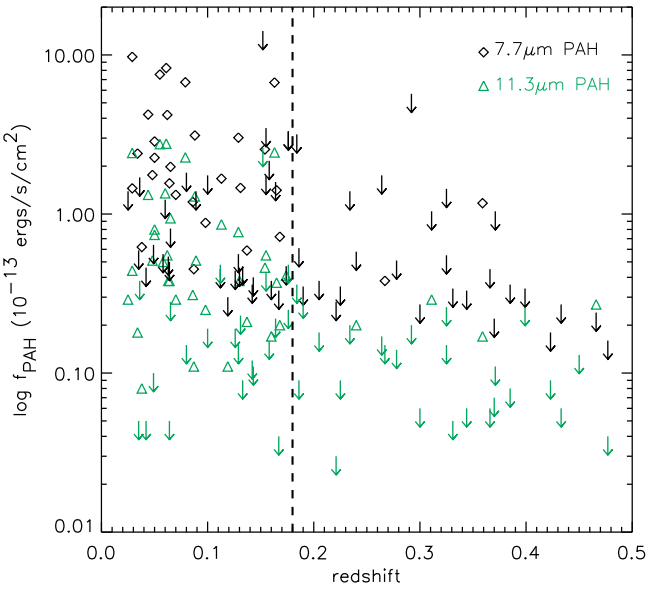

Figure 1. PAH flux versus redshift for the PG QSOs from Shi et al. (2007). Black diamonds and black upper limits are for the 7.7 μm PAH feature. Blue triangles and blue upper limits are for the 11.3 μm PAH feature. Note that above $z = 0.18$ (dashed line) the PAH detections are severely incomplete – this serves as a cut for our sample.

In line with the criteria outlined above, our sample consists of Palomar–Green (PG) QSOs with mid-IR spectroscopy, drawn from Shi et al. (2007). PG QSOs are selected in the *B* band, have blue $U - B$ colours, a star-like appearance and broad emission lines; see Schmidt & Green (1983). Shi et al. (2007) present mid-IR *Spitzer*/IRS spectra and examine the mid-IR and SF properties for the entire parent PG QSO sample up to $z = 0.5$ (see also Schweitzer et al. 2006; Netzer et al. 2007; Veilleux et al. 2009). Since the availability of PAH flux measurements is central to our work, in order to determine the redshift range for our sample we examine the distribution of PAH fluxes as a function of redshift (Fig. 1). It is clear that above $z = 0.18$ the PAH detections are sparse, hence we subsequently select PG QSOs at $z < 0.18$ (58 sources).

2.2 PAH-derived SFRs

PAH features appearing in the mid-IR 6–13 μm (e.g. Allamandola, Tielens & Barker 1985, 1989; Laurent et al. 1999, Sturm et al. 2000) have been detected in a wide range of sources and used as diagnostic tools for physical processes in the interstellar medium; they are thought to originate in photodissociation regions and are excited by UV photons from massive young stars (e.g. Roche & Aitken 1985; Roche et al. 1991; Li & Draine 2002). As a result, PAHs are extensively used as star formation tracers (e.g. Förster Schreiber et al. 2004; Peeters, Spoon & Tielens 2004; Risaliti et al. 2006; Pope et al. 2008) and although the properties of the PAH spectrum vary over small scales and are affected by factors such as metallicity and radiation field hardness (e.g. Roche et al. 1991; Bendo et al. 2008; Engelbracht et al. 2008; Gordon et al. 2008) they are good gauges of star formation on galactic scales (Roussel et al. 2001; Kennicutt et al. 2009; Treyer et al. 2010) and have been seen to correlate well with other star formation tracers such as H α (e.g. Kennicutt et al. 2009), [Ne II] (e.g. Ho & Keto 2007; Shipley et al. 2013) and the total infrared luminosity ($L_{\rm IR}$; e.g. Peeters et al. 2004; Brandl et al. 2006, Hanami et al. 2012). Although PAHs are prevalent in SFGs, early studies of AGN mid-IR spectra reported a lack of PAH features around some AGN (e.g. Aitken & Roche 1985; Roche et al. 1991), which led to the idea that PAHs might be destroyed by hard radiation from the AGN (e.g. Aitken & Roche 1985; Voit 1992). However, subsequent studies have shown that PAHs are common features in galaxies which host AGN and as such they have been routinely employed as star formation tracers in AGN hosts (e.g. Shi et al. 2007; Lutz et al. 2008; Watabe, Kawakatu & Imanishi 2008; Rawlings et al. 2013; Esquej et al. 2014).

Shi et al. measure the strength of the 7.7 and 11.3 μm PAH emission features in the PG QSO spectra used in this work and derive the conversion factor between PAH luminosity and 8–1000 μm total infrared luminosity attributed to star formation ($L_{\rm SFIR}$) for each PG QSO, by adopting an SED template from the work of Dale et al. (2001) and Dale & Helou (2002) that gives the closest PAH emission line flux at the redshift of the object; see Shi et al. (2007) for more details. We note that the $L_{\rm SFIR}/L_{\rm PAH}$ conversions in Shi et al. are consistent with other works, e.g. Lutz et al. (2003), Smith et al. (2007) and Hernán-Caballero et al. (2009). In cases where both 7.7 and 11.3 μm PAH features are detected, Shi et al. (2007) use the 11.3 μm PAH to derive $L_{\rm SFIR}$ as its uncertainty is lower than that of the 7.7 μm PAH and it is thought to be less susceptible to suppression by the AGN radiation (e.g. see Smith et al. 2007; O'Dowd et al. 2009; Diamond-Stanic & Rieke 2010; ; Hunt et al. 2010; Esquej et al. 2014; Shi et al. 2014). In our final sample (Section 2.4), there is only one source for which $L_{\rm SFIR}$ is derived using the 7.7 μm PAH instead of the 11.3 μm one, as the latter is not detected (in Section 4.1.2 we examine the effect this has on our results).

2.3 Photometric data

We obtain archival and published photometry for the 58 $z < 0.18$ PG QSOs as follows: Palomar *B*-band photometry (Shi et al. 2014; see also Schmidt & Green 1983), SDSS magnitudes from the SDSS Photometric Catalog, Release 9 (Ahn et al. 2012), 2MASS magnitudes from the 2MASS All-Sky Catalog of Point Sources (Skrutskie et al. 2006), *WISE* magnitudes from the AllWISE Source Catalog,[1] *Spitzer*/MIPS data from Shi et al. (2014), ISO flux densities (Haas et al. 2000, 2003), *IRAS* photometry from the *IRAS* point source and faint source catalogues, *AKARI* 9 and 18 μm data from the *AKARI*/IRC mid-IR all-sky Survey and *AKARI*/FIS All-Sky Survey Point Source fluxes at 65, 90, 140, 160 μm, *Herschel* (Pilbratt et al. 2010)[2]/PACS (Poglitsch et al. 2010) 160 μm flux densities from Shi et al. (2014) and radio data from Haas et al. (2003). The *Herschel*/SPIRE (Griffin et al. 2010) data are from the *Herschel* Science Archive, processed by the SPIRE HIPE pipeline version 12 (Ott 2010). The photometry was extracted at the source position using the SUSSEXTractor task within HIPE (Savage & Oliver 2007, Smith et al. 2012, Pearson et al. 2014). The SUSSEXtractor task estimates the flux density from an image smoothed with a convolution kernel derived from the SPIRE beam full width at half-maximum. In the cases where our targets were observed in the SPIRE small map mode, the flux density measured by SUSSEXtractor was verified using the SPIRE Timeline Fitter (Bendo et al. 2013) which fits a two-dimensional elliptical Gaussian function at the source position in the timeline data. The agreement between the SUSSEXtractor and Timeline Fitter flux densities was found to be better than ∼5 per cent.

The detection statistics are as follows: four sources have no significant detections above 25 μm (∼7 per cent of the sample) and five sources have no significant detections above 100 μm (∼9 per cent). These nine sources also have upper limits in $L_{\rm SFIR}$; in total there are 21 sources with upper limits in $L_{\rm SFIR}$ (∼36 per cent of the sample).

We calculate rest-frame 5100 Å luminosities (νL_ν), by interpolating between the SDSS bands. For the nine objects which do not have SDSS counterparts, we interpolate between the Palomar *B* band and the 2MASS *J* band. To convert to big blue bump luminosities ($L_{\rm BBB}$, 2keV–1 μm; Grupe et al. 2010), we use the Grupe et al. (2010) expression, $\log L_{\rm BBB} = (1.32 \pm 0.06) \times \log \nu L_{\nu,\,5100} - (10.84 \pm 2.21)$. The range in $\nu L_{\nu,\,5100}$ covered by our sample is three orders of magnitude (10^{43}–10^{46} erg s^{-1}; see Fig 2), translating to $\log [L_{\rm BBB}\ ({\rm erg\ s^{-1}})] = 44.5$–48, and is a strong function of

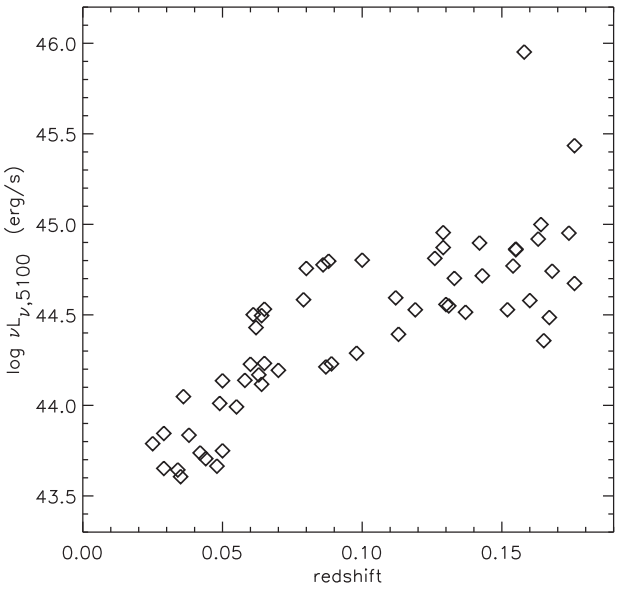

Figure 2. Rest-frame luminosity at 5100 Å ($\nu L_{\nu,5100}$, erg s^{-1}) as a function of redshift for the sample of 58 PG QSOs at $z < 0.18$.

[1] http://wise2.ipac.caltech.edu/docs/release/allwise/

[2] *Herschel* is an ESA space observatory with science instruments provided by European-led Principal Investigator consortia and with important participation from NASA.

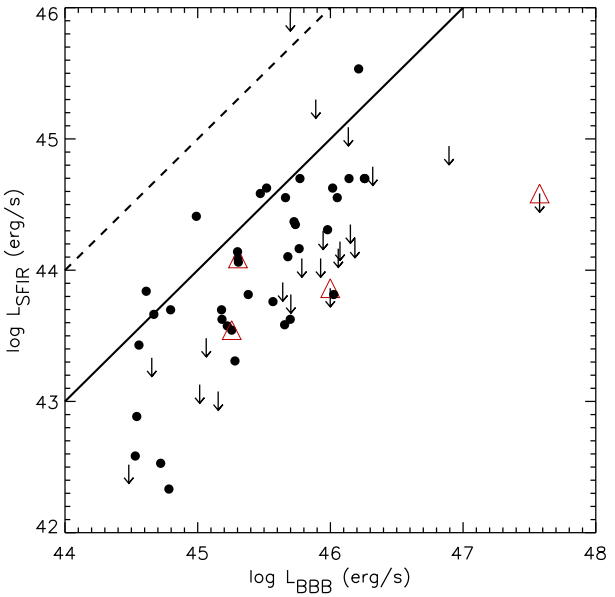

Figure 3. Total infrared luminosity attributed to star formation ($L_{\rm SFIR}$; 8–1000 μm) versus AGN big blue bump luminosity ($L_{\rm BBB}$; 2 keV–1 μm) for the 58 PG QSOs at $z < 0.18$. The dashed line is the one-to-one relation and the solid line represents $L_{\rm BBB} = 10 \times L_{\rm SFIR}$. Red triangles indicate the radio-loud sources. Our final sample includes all objects below the solid line apart from the ones that are identified as radio-loud.

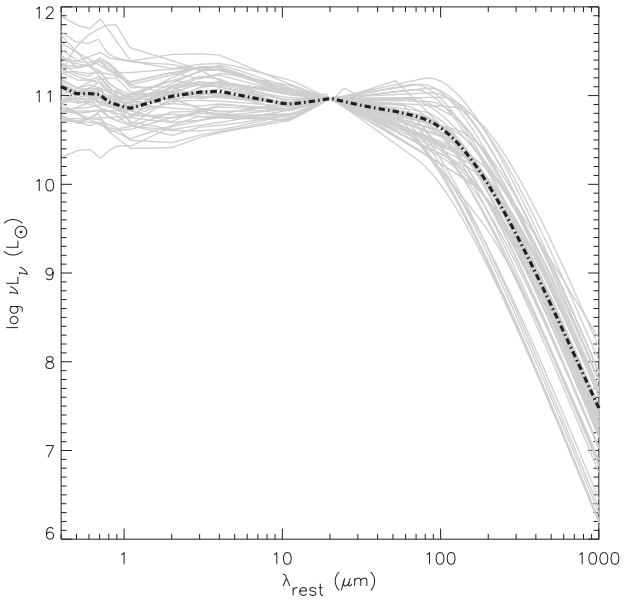

Figure 4. The average SED of the sample of 47 QSOs (black dot–dashed curve). The average SED is plotted in actual luminosity units, whereas the individual QSO SEDs (grey curves) are normalized to the average SED at 20 μm.

redshift. According to the local AGN optical luminosity function of Schulze, Wisotzki & Husemann (2009), our sample covers the whole luminosity range above $L_\star$, hence corresponds to the most luminous nearby AGN.

2.4 The final sample

Fig. 3 shows $L_{\rm SFIR}$ (the total infrared luminosity attributed to star formation) as a function of $L_{\rm BBB}$. Note that all bar one source have $L_{\rm BBB} > L_{\rm SFIR}$ and for the majority $L_{\rm BBB} > 10 \times L_{\rm SFIR}$. This confirms the suitability of this sample for our study, i.e. sources where the AGN is more powerful than the galaxies' stellar output. For our analysis, we keep the sources with $L_{\rm BBB} > 10 \times L_{\rm SFIR}$, where the AGN is an order of magnitude more luminous than the luminosity from star formation. In this way, we maximize the ratio of AGN to stellar powered emission.

We remove radio-loud AGN from our final sample as their far-IR emission is contaminated by non-thermal processes. Kellermann et al. (1989) examine the radio-loudness of the PG sample, using a radio loudness criterion (R) defined as the ratio of radio flux at 6 cm to optical flux at 4400 Å. We take $R = 10$ as the dividing line between radio-quiet and radio-loud AGN. Four sources are identified as radio-loud.

The final sample consists of 47, radio-quiet PG QSOs at $z < 0.18$, with $L_{\rm BBB} > 10 \times L_{\rm SFIR}$. Hereafter, our analysis involves only the final sample.

3 METHOD AND RESULTS

3.1 Fitting QSO SEDs

We do the SED fitting as follows: from 22 μm onwards (just after the 18 μm silicate feature), we fit with a power-law (PL)/greybody (GB) combination, whereas up to 22 μm we interpolate logarithmically between the bands. The fitting includes the GB function for the far-IR to describe the emission from large grains in equilibrium, and a PL for the mid-IR to approximate the emission from hot dust, combined at a critical frequency ν_* (see also Blain, Barnard & Chapman 2003; Younger et al. 2009) as follows:

$$F_\nu \propto \begin{cases} \dfrac{\nu^{3+\beta}}{e^{(h\nu/kT_{\rm dust})}-1} & \text{if} \quad \nu < \nu_* \\ \nu^{\alpha} & \text{if} \quad \nu > \nu_*, \end{cases} \tag{1}$$

where F_ν is the flux density, h is the Planck constant, c is the speed of light in a vacuum, k is the Boltzmann constant, $T_{\rm dust}$ is the temperature of the GB function and β is the emissivity – we adopt $\beta = 1.5$, consistent with studies of the far-IR emissivity of large grains (Desert, Boulanger & Puget 1990; see also Boselli et al. 2012). At the critical frequency ν_*, the slopes of the two functions are equal and hence $\alpha = {\rm dlog\,GB/dlog}\nu$. We perform χ^2 fitting in order to find the best-fitting GB/PL combination, with α, ν_* and $T_{\rm dust}$ as free parameters. The SEDs for all 47 sources in our final sample are shown in Fig. 4 normalized at 20 μm, and also individually in Appendix A. The small peak at 20 μm is the silicate feature in emission (see Shi et al. 2014). This is quite common in unobscured QSOs, as the emission from silicates in the inner part of the torus is visible (e.g. Siebenmorgen et al. 2005; Sturm et al. 2005, Shi et al. 2006). Note that our SEDs can be considered well sampled up to about 500 μm (rest frame).

3.2 Matching SF templates to QSOs

We now assign a SF SED template to each PG QSO. As these are low-redshift systems, dust temperature evolution is not significantly at play (see Symeonidis et al. 2013a), hence it is appropriate to use SED templates for nearby galaxies. To be consistent with how the $L_{\rm SFIR}$ values were derived in Shi et al. (2007; see Section 2.2), we use the Dale & Helou (2002; hereafter DH02) SED library. As in Shi et al., we assign total infrared luminosities ($L_{\rm IR}$, 8–1000 μm) to the DH02 SED library using their 60/100 μm colour and the

relation in Marcillac et al. (2006). Each SED template is subsequently normalized to units of $L_{\odot}$ by its $L_{\rm IR}$. For each PG QSO, we chose the DH02 template whose $L_{\rm IR,\,templ}$ is closest to the QSO's $L_{\rm SFIR}$ calculated by Shi et al. (2007). This is an important step as there is a correlation between $L_{\rm IR}$ and dust temperature (or SED peak, e.g. Dunne et al. 2000; Dale et al. 2001; see also Symeonidis et al. 2013a), so for each PG QSO we need to have the appropriate far-IR shape of SF emission.

For each QSO, the corresponding DH02 template is scaled by the factor $L_{\rm SFIR}/L_{\rm IR,\,templ}$. For the 17 sources (out of 47, 36 per cent) which have a 3σ upper limit in $L_{\rm SFIR}$ due to low significance PAH detections, we assume that their $L_{\rm SFIR}$ is equal to half the upper limit and scale the corresponding DH02 templates by the factor $\frac{L_{\rm SFIR,lim}/2}{L_{\rm IR,templ}}$. This is a reasonable assumption given that they could in principle have any $L_{\rm SFIR}$ from 0 to $L_{\rm SFIR,\,lim}$; in Section 3.4, we evaluate the effect that this has on our results.

3.3 The intrinsic AGN SED

Our PG QSO SEDs are broad-band, hence to subtract the SF DH02 templates which include spectral data in the mid-IR, we resample the 2–30 μm part of the rest-frame DH02 SED into *WISE* filter-convolved luminosities at 3.4, 4.6, 12 and 22 μm and interpolate between them. The average SF SED is then subtracted from the average PG QSO SED from 5 μm onwards, which is the onset of the dust continuum; the residual we obtain is the average *intrinsic* or *pure* AGN SED. We confirm that we get the same intrinsic AGN SED if instead we calculate the residual SED for each PG QSO and subsequently average those. Note that our intrinsic AGN SED can be considered well sampled up to about 500 μm (rest frame).

In Appendix C, we test the method used to calculate the average SF infrared SED for our sample of QSOs (see this section and Section 2.2), on two sets of pure starburst galaxies with known far-IR SEDs. We find that the average far-IR SED of each set of starbursts is reproduced correctly, and thus we have confidence that this method accurately predicts the average SF SED corresponding to the input PAH measurements.

The matched SF templates and QSO SEDs are shown in Fig. 5 split into two luminosity groups each covering about 1.5 dex in $L_{\rm BBB}$ above and below $\log L_{\rm BBB} = 45.5$ and then all together. Note that shortwards of about 20 μm, the average QSO SED is typically at least an order of magnitude brighter than the average SF SED and the AGN entirely dominates the broad-band emission, whereas longwards of 20 μm there is an additional contribution from the host galaxy. The lower panel shows that the average luminosity from star formation is less than the average intrinsic AGN luminosity up to ∼100 μm and approximately equal to it thereafter, suggesting that in some of these sources the whole SED is AGN-dominated.

Fig. 6 compares the intrinsic AGN SEDs for the two QSO luminosity bins, $\log \nu L_{\nu,\,BBB} < 45.5$ and $\log \nu L_{\nu,\,BBB} > 45.5$ normalized at 20 μm, where the SEDs change from AGN dominated to AGN+host. We note that there is a small difference in the 1–10 μm region between the low-luminosity and high-luminosity QSOs of about 0.2 dex, with the more luminous sources having a more pronounced 1–10 μm bump in that wavelength range. Such a mid-IR bump has been observed before in luminous AGN; e.g. Leipski et al. (2014) find that a separate hot blackbody component ($T \sim 1200$ K) is needed to fit the 1–10 μm SED of their QSO sample. Emission from the accretion disc is not significant past 1 μm (e.g. Laor 1990; Collinson et al. 2015), so this feature is likely caused by scattered and reprocessed emission by dust (e.g. see also models by Fritz,

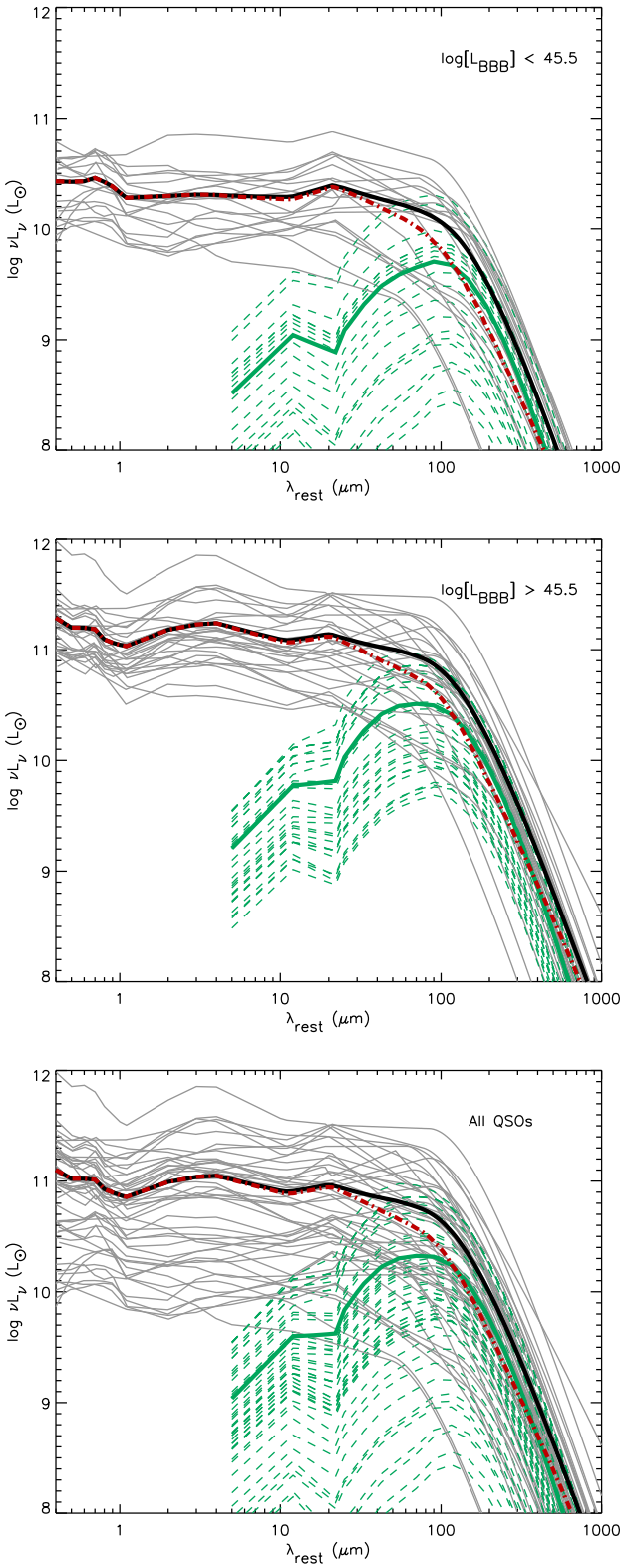

Figure 5. SEDs for the PG QSOs in our sample (black curves) and their average (thick black curve), as well as the SF templates (green dashed curves) and their average (thick green curve). The intrinsic AGN SED is shown by the red dot–dashed curve and is obtained by subtracting the thick green curve from the thick black curve. In the first two panels, the sample is split into two AGN luminosity bins: $\log [L_{\rm BBB}] < 45.5$ and $\log [L_{\rm BBB}] > 45.5$ and the last panel shows all QSOs together.

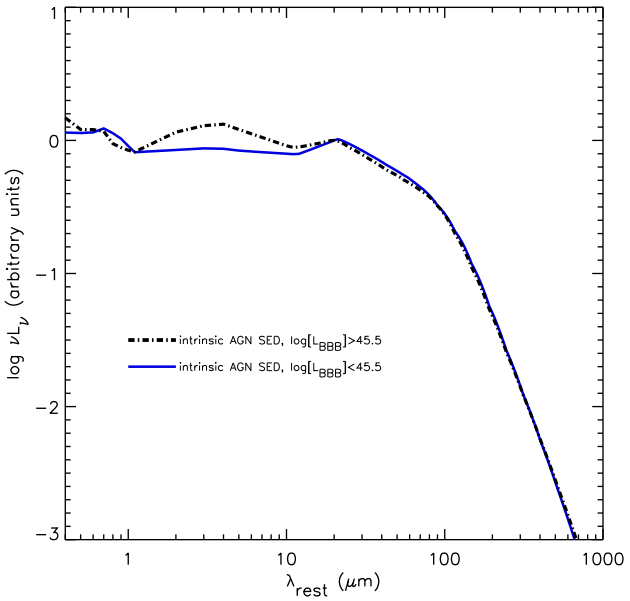

Figure 6. The intrinsic AGN SED derived separately from the log [$L_{\rm BBB}$] < 45.5 and log [$L_{\rm BBB}$] > 45.5 QSOs, normalized at 20 μm.

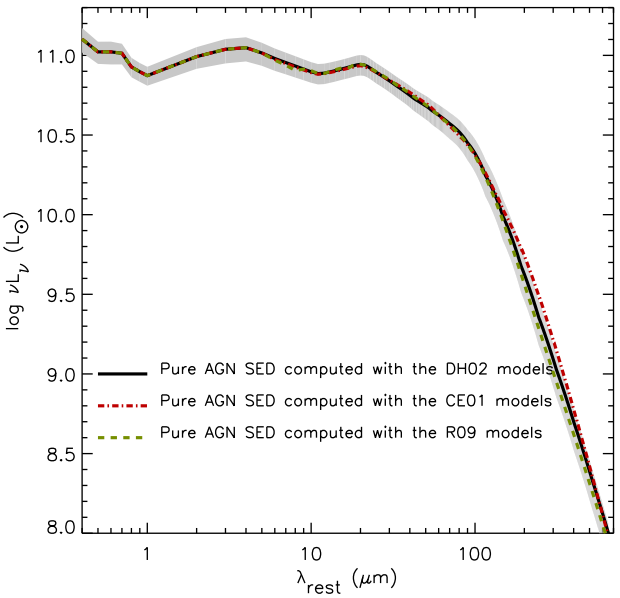

Figure 7. The intrinsic AGN SED computed with DH02 library (solid black curve and 68 per cent confidence intervals shown as a shaded region), compared with the one computed with the Chary & Elbaz 2001 (CE01) and Rieke et al. 2009 (R09) SED templates – see Section 3.3. Note that throughout this work, we use the one computed with the DH02 library, although the difference is small between the three SEDs.

Franceschini & Hatziminaoglou 2006). In contrast to the mid-IR, there is negligible difference in the intrinsic SEDs of the lower and higher luminosity AGN longwards of 20 μm. In the remainder of this work, we use the intrinsic AGN SED derived from the whole sample (see lower panel of Fig. 5) and publish this in Table D1.

To calculate the 68 per cent confidence intervals on the intrinsic AGN SED, we bootstrap the residual SEDs of our sample of 47 QSOs and hence re-derive an intrinsic AGN SED 5000 times. Since $L_{\rm SFIR}$ is used to assign an SF template, which is in turn used to compute the residual SEDs, the uncertainties on $L_{\rm SFIR}$ (which are a combination of the $L_{\rm SFIR}/L_{\rm PAH}$ conversion factor uncertainties and PAH flux measurement errors) are propagated to the residual SEDs. The distribution of *observed* residual SEDs is thus the result of the convolution of the *intrinsic* distribution of residual SEDs and the error distribution and is consequently broader than the intrinsic distribution. Since the bootstrapping is performed on the observed distribution of residual SEDs, the resulting error on the mean has all random errors folded in. We find that the 1σ error on the pure AGN SED ranges between 12 and 45 per cent as a function of wavelength (see Fig. 12).

3.4 Effect of PAH upper limits on the intrinsic AGN SED

We remind the reader that for the sources which have low significance PAH detections, we have taken $L_{\rm SFIR} = L_{\rm SFIR,\,lim}/2$ (see Section 3.2). We now examine how the intrinsic AGN SED changes if we set $L_{\rm SFIR}$ to the minimum and maximum values, i.e. $L_{\rm SFIR} = 0$ and $L_{\rm SFIR} = L_{\rm SFIR,\,lim}$. We find that the pure AGN SED changes by up to 30 per cent in the 20–1000 μm range, within the 68 per cent confidence intervals we obtain from bootstrapping.

3.5 Effect of SED library choice on the intrinsic AGN SED

We assess the effect of our choice of SF SED library, by re-computing the intrinsic AGN SED with two different SF SED libraries, the Rieke et al. (2009) templates and the Chary & Elbaz (2001) templates (note that the Rieke et al. library does not extend to log [$L_{\rm IR}/{\rm L}_{\odot}$] < 9.75, so we assign the log [$L_{\rm IR}/{\rm L}_{\odot}$] < 9.75 template to all our $L_{\rm SFIR} < 10^{10}$ L $_{\odot}$ sources). Fig. 7 shows that there is small difference in the resulting intrinsic AGN SED.

4 DISCUSSION

We found that the average intrinsic AGN emission in a sample of nearby QSOs dominates the broad-band SED up to about 100 μm and is comparable to the average SF emission thereafter. Before we examine the implications of our results in Sections 4.2 and 4.4, we dedicate Section 4.1 to a discussion regarding the SF luminosities in our sample of PG QSOs.

4.1 Considerations on the SF luminosities of QSO host galaxies

Recently, Petric et al. (2015) reported their results on the far-IR emission of PG QSOs, finding an offset between IR SED-derived SFRs and PAH-derived SFRs, with the former being systematically larger. This result is consistent with ours, i.e. that the star formation implied by PAHs does not account for all the far-IR emission in nearby QSOs. Petric et al. (2015) suggest that as well as the heating of dust by the AGN, heating of the dust by old stars, and suppression of the PAHs by the AGN may be important.

4.1.1 Could evolved stars contribute to dust heating?

In some nearby low-luminosity, low-SFR galaxies, a fraction of the far-IR emission is heated by the evolved stellar population rather than young stars (e.g. Bendo et al. 2010, 2012, 2015). This suggests that for the eight QSOs in our sample with measured $L_{\rm SFIR} < 10^{10}\,{\rm L}_{\odot}$, scaling the templates according to $L_{\rm SFIR}$ might underestimate the normalization of the template with respect to the QSO SED. Nevertheless, the $L_{\rm SFIR}$ of these QSOs is very low compared

to the average $L_{\rm SFIR}$ of the sample, thus even increasing the normalization by a factor of 3 (corresponding to an extreme case whereby only 30 per cent of the total IR luminosity is due to dust heated by star formation; see Bendo et al. 2015) has a negligible effect on our intrinsic AGN SED.

4.1.2 How well do PAHs trace star formation in AGN host galaxies?

PAH molecules are not expected (or observed) to survive in the vicinity of the AGN, where they are directly illuminated by its hard radiation field (Siebenmorgen, Krügel & Spoon 2004). However, there has been a long-standing debate about whether PAHs are suppressed further out in the host galaxies of AGN, where the ultraviolet radiation field is dominated by stars. In theory, X-rays from the AGN are expected to destroy PAHs as a consequence of photoionization, the relevant transition being the carbon K edge at 0.288 keV in the soft X-rays (Voit 1992). The PAH survival condition suggested by Voit (1992) is that PAHs containing $\gtrsim$50 carbon atoms can survive at $\sim$1 kpc from an AGN of X-ray luminosity $\nu L_\nu = 10^{44}$erg s^{-1} if they are shielded from the AGN by column densities $>10^{22}$ cm^{-2}. Typically, AGN tori have column densities more than an order of magnitude larger than this (e.g. Risaliti, Maiolino & Salvati 1999; Buchner et al. 2014) and their covering factors are 50 per cent or more (e.g. Maiolino & Rieke 1995; Dwelly & Page 2006). In addition, observational evidence suggests that AGN tori are aligned with the galaxy plane (e.g. Maiolino & Rieke 1995; Lagos et al. 2011). As a result, PAHs in SF regions are likely to be well shielded by the torus along the majority of lines of sight in the galaxy.

Some studies argue that the smaller PAH molecules responsible for the shorter wavelength PAH features might be suppressed in the host galaxies of AGN, but there is strong empirical evidence that this is not the case for the 11.3 μm feature. For example, Smith et al. (2007) find that in their *Spitzer* study of 59 nearby galaxies, some that host AGN have lower ratios of 7.7–11.3 μm PAH emission than those that do not, and with a more pronounced trend closer to the nuclei of the galaxies. O'Dowd et al. (2009) show a similar trend of reduced 7.7 μm PAH emission in some of the AGN-hosting members of their sample of 92 $z \sim 0.1$ galaxies. They argue that the molecules responsible for the 7.7 μm emission are likely to be susceptible to destruction by X-rays or shocks from the AGN, but that the 11.3 μm emission is likely to come from larger molecules that are more resilient. Subsequently, Diamond-Stanic & Rieke (2010) studied a sample of 35 Seyfert galaxies and showed that while the shorter wavelength PAH features are suppressed in some of these objects, the 11.3 μm emission obeys the same relationship with [Ne II] as purely SF objects, implying that it is a robust tracer of SFR regardless of the presence of an AGN. Finally, Shipley et al. (2013) conclude that the AGN do not affect PAHs on galaxy-wide scales based on the lack of any trend between the $L_{\rm PAH(7.7)}/L_{\rm PAH(11.3)}$ ratio and the AGN luminosity or hardness of the radiation field.

Only one object (PG 0838+770) in our sample of nearby PG QSOs has $L_{\rm SFIR}$ value based on the 7.7 μm PAH rather than the 11.3 μm feature. Noting the potential suppression of 7.7 μm PAH features by AGN, we have checked the extent to which the inclusion of this object affects our intrinsic AGN SED by re-computing the SED with this object excluded from the sample. We find that the intrinsic AGN changes by less than 1.4 per cent; see Fig. 8.

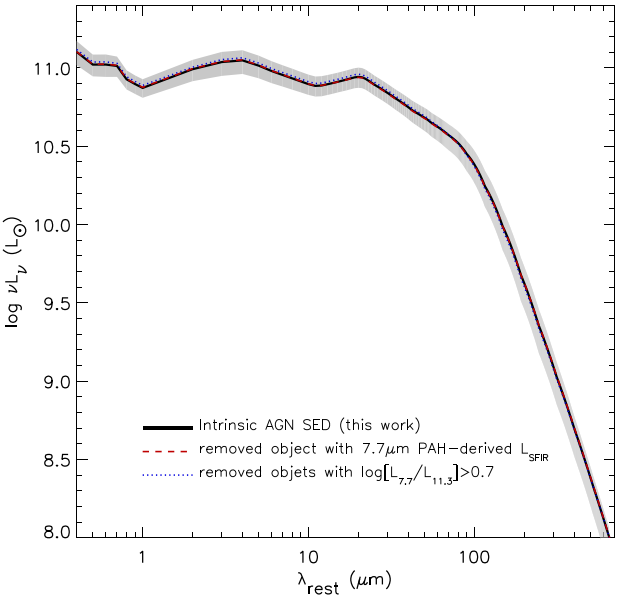

Figure 8. The intrinsic AGN SED (solid black curve and 68 per cent confidence intervals shown as a shaded region), re-computed without the object with a 7.7 μm PAH-derived $L_{\rm SFIR}$ (red dashed curve) and without the five objects with elevated $L_{\rm PAH(7.7)}/L_{\rm PAH(11.3)}$ ratios (blue dotted curve); note that the three curves are almost indistinguishable.

Ground-based studies using 8–10 m telescopes have allowed the PAH emission from the host galaxies of nearby AGN to be studied at much higher spatial resolution than the space-based studies. Recently, Esquej et al. (2014) examined the PAH emission from a sample of 29 Seyfert galaxies and found no evidence for the suppression of the 11.3 μm emission even within a few tens of pc from the nucleus. Alonso-Herrero et al. (2014) find in their study of six local AGN that 11.3 μm emission is seen at 10 pc from the nucleus, suggesting that the molecules responsible for this emission feature are robust to AGN destruction even in the innermost regions of the host galaxy. In a follow up case study of the nearby Seyfert Mrk 1066, Ramos-Almeida et al. (2014) explicitly calculate that when the nuclear continuum is subtracted, the equivalent width of the 11.3 μm PAH emission in the inner region of this galaxy is consistent with that seen in SF regions, supporting the validity of the 11.3 μm emission as a tracer of the SFR in AGN host galaxies.

On the other hand, one study has raised concerns about the use of the 11.3 μm feature in AGN hosts. LaMassa et al. (2012) find that a number of sources in their sample of Seyfert 2 galaxies show abnormally large ratios of 7.7–11.3 μm PAH emission. LaMassa et al. (2012) interpret these ratios as evidence for suppression of the 11.3 μm PAH emission by the AGN, though extinction offers an alternative explanation for large 11.3 μm/7.7 μm PAH ratios, as noted by Diamond-Stanic & Rieke (2010). We compare the distribution of the $L_{\rm PAH(7.7)}/L_{\rm PAH(11.3)}$ ratio in our sample of PG QSOs with that of the local star forming galaxies samples of Brandl et al. (2006), LaMassa et al. (2012) and Stierwalt et al. (2014), and find them to be broadly consistent with only five PG QSOs having elevated $L_{\rm PAH(7.7)}/L_{\rm PAH(11.3)}$ ratios, higher than the typical values seen in SFGs (i.e. log $[L_{\rm PAH(7.7)}/L_{\rm PAH(11.3)}] > 0.7$). We check the extent to which inclusion of the five objects with elevated $L_{\rm PAH(7.7)}/L_{\rm PAH(11.3)}$ (PG 0838+770, PG 1115+407, PG 1310−108, PG 1535+547, PG 2130+099) affects our results, by re-computing the intrinsic AGN SED with these objects excluded. The resulting SED differs at most by 5.1 per cent from that derived from the whole sample;

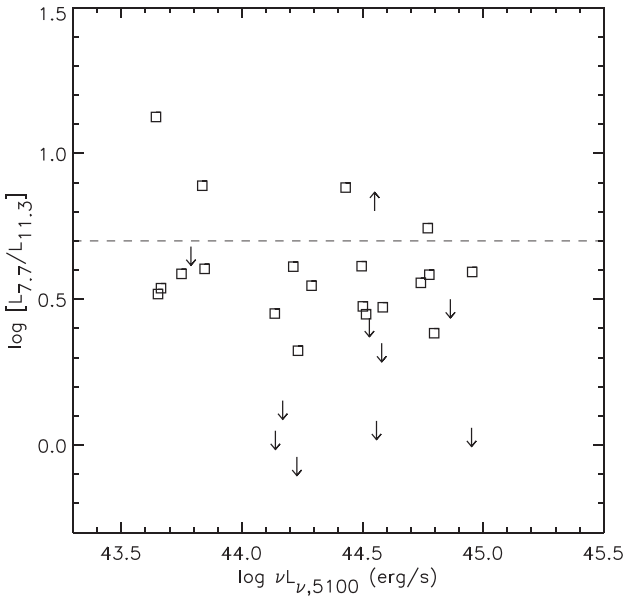

Figure 9. Plot of the 7.7/11.3 μm ratio as a function of AGN luminosity (at 5100 Å). Only objects for which at least one of the features is detected are shown. Squares are objects with both features detected, upper limits are for the objects for which the 7.7 μm feature is not detected and the lower limit is for the object with undetected 11.3 μm PAH. Above the dashed line at log $[L_{\rm PAH(7.7)}/L_{\rm PAH(11.3)}] > 0.7$, we consider the QSOs to have elevated $L_{\rm PAH(7.7)}/L_{\rm PAH(11.3)}$ ratios, higher than the typical values seen in SFGs.

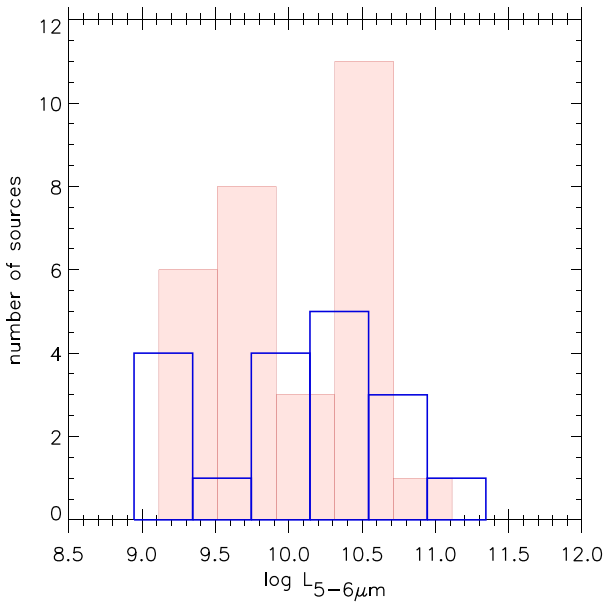

Figure 10. The distribution in QSO luminosity (integrated in the 5–6 μm region; values taken from Shi et al. 2007) for our sample, split into sources which have PAH detections (red filled histogram) and sources which have no PAH detections (blue histogram).

see Fig 8. Finally, we inspect the 7.7 μm/11.3 μm PAH luminosity ratio as a function of AGN luminosity (at 5100 Å) for our sample of QSOs (Fig. 9, note only objects with at least one PAH detection are shown). We see no trend between the $L_{\rm PAH(7.7)}/L_{\rm PAH(11.3)}$ ratio and AGN luminosity for the PG QSOs with elevated $L_{\rm PAH(7.7)}/L_{\rm PAH(11.3)}$. Whatever the reason is for the elevated 7.7 μm/11.3 μm PAH ratios in these five objects, they do not have a significant impact on the results.

We also investigate the concern raised by Petric et al. (2015), that the 11.3 PAH detection rate is lower for the most IR-luminous AGN, which might arise as a result of AGN suppression of the 11.3 μm PAH emission. For our sample of QSOs, we show in Fig. 10 the distributions in $L_{5-6\,\mu\rm m}$ luminosity (i.e. the integrated luminosity in the 5–6 μm range), for sources which have 11.3 μm PAH detections and those that do not. The values of $L_{5-6\,\mu\rm m}$ were taken from Shi et al. (2007). We find no offset in the two distributions, indicating that the 11.3 μm PAH detection rate is not dependent on AGN luminosity.

The SEDs constructed separately for the QSOs with log $[L_{\rm BBB}]$ above and below 45.5 (Figs 5 and 6), offer another opportunity to examine the possibility that the 11.3 μm PAH emission is suppressed by the AGN. If the AGN were suppressing the 11.3 μm emission, we would expect a larger effect in the higher luminosity subset: the stronger AGN radiation field would produce stronger suppression of the 11.3 μm emission, so that the SFR would be systematically underestimated by a larger degree in the more luminous QSOs, which would translate to a larger flux at long wavelengths (>70 μm) in the intrinsic AGN SED for the more luminous QSOs than for the less luminous QSOs. Instead, the shapes of the intrinsic AGN SEDs for the higher and lower luminosity subsamples are almost indistinguishable beyond 20 μm (Fig. 6), and hence no evidence for the suppression of 11.3 μm PAH emission by the AGN can be found in the comparison.

To summarize, a number of studies in the literature provide strong evidence that the 11.3 μm PAH offers a robust measure of star formation in AGN host galaxies, even in the circumnuclear regions. Only four of our sample of QSOs show the elevated 7.7 μm/11.3 μm PAH ratios which LaMassa et al. (2012) attribute to AGN-suppression of 11.3 μm PAH emission, and excising these objects from our sample has no significant impact on our intrinsic AGN SED. There is no trend in our sample between elevated 7.7 μm/11.3 μm PAH ratios and AGN luminosity; indeed, most of the sources in our sample show 7.7 μm/11.3 μm PAH ratios which are consistent with those found in SFGs. We also find no evidence for AGN suppression of the 11.3 μm emission when we compare the higher and lower AGN-luminosity subsets of our sample. The star formation contribution to the average SED appears to be robust to any effect of the AGN on the 11.3 μm PAH emission, and hence the intrinsic AGN SED appears to be likewise robust to any such effect.

4.2 Comparison with other AGN SEDs

In Fig. 11, we compare the average SED of our sample of QSOs (i.e. AGN+host, also shown in Fig. 4) to the average QSO SEDs from Elvis et al. (1994), Richards et al. (2006), Shang et al. (2011) and the type I QSO and type II QSO templates from the SWIRE template library[3] (Polletta et al. 2006, 2007). Our QSO SED agrees well with the SWIRE type I QSO SED, particularly in the far-IR/submm, whereas it has less far-IR/submm power than the type II QSO SWIRE SED, likely due to a different amount of host galaxy contribution. On the other hand, the composite SEDs of Elvis et al. (1994), Richards et al. (2006) and Shang et al. (2011) fall short of our SED in the 60–300 μm region. However, note that their data do not probe the submm and hence the SEDs are extrapolated in that wavelength range. Most of the Elvis et al. QSOs are not significantly

[3] http://www.iasf-milano.inaf.it/~polletta/templates/swire_templates.html

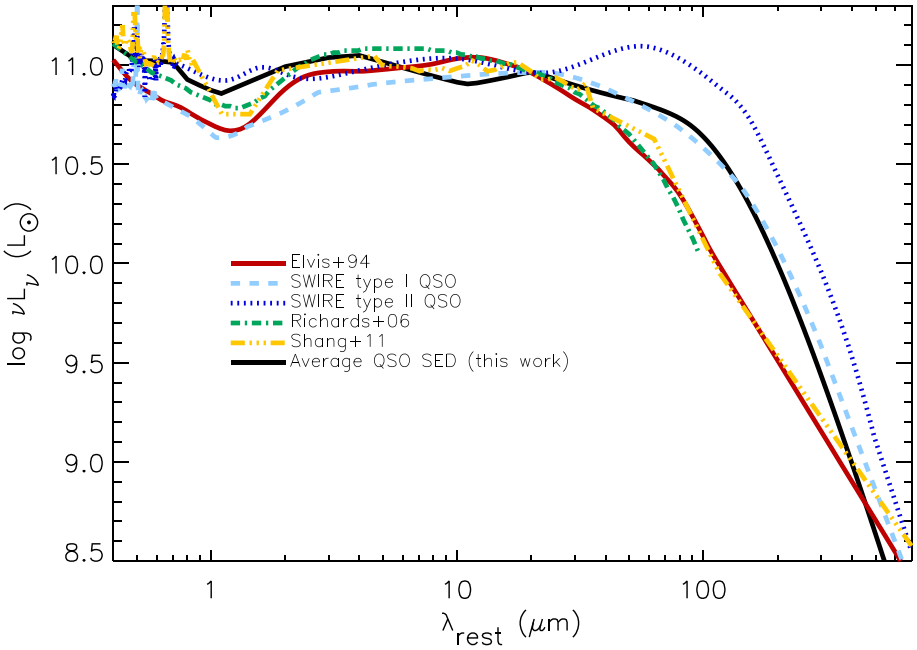

Figure 11. The average QSO SED of our sample (black solid line), compared to those from Elvis et al. (1994), Richards et al. (2006), Shang et al. (2011) and the SWIRE template library are also included, normalized at 20 μm.

detected at *IRAS*/100 μm and a large fraction (∼25 per cent) are not significantly detected at *IRAS*/60 μm. Similarly, only a handful of the Richards et al. QSOs have 70 μm data. With respect to the Shang et al. radio-quiet SED, again their data probe shorter rest-frame wavelengths both as a consequence of their sample extending to much higher redshift and the lack of far-IR photometry for about half of the sources.

Fig. 12 compares the intrinsic AGN SED extracted here to the SEDs from Netzer et al. (2007) and Mullaney et al. (2011), both of which are classed as pure AGN SEDs. The intrinsic AGN SED (in νL_ν) we derive in this work can be considered 'flat' within 0.2 dex up to about 20 μm, with a subsequent slow drop off of ∼0.4 dex from 20 to 60 μm and ∼0.3 dex from 60 to 100 μm. Fig. 12 shows that the Netzer et al. and Mullaney et al. SEDs are much steeper in the far-IR than ours, particularly the former whose emission at 70 μm is more than half a dex lower. The Netzer et al. AGN SED was derived for a subsample of PG QSOs which were studied as part of the *Spitzer* QUASAR and ULIRG evolution study (QUEST; Schweitzer et al.

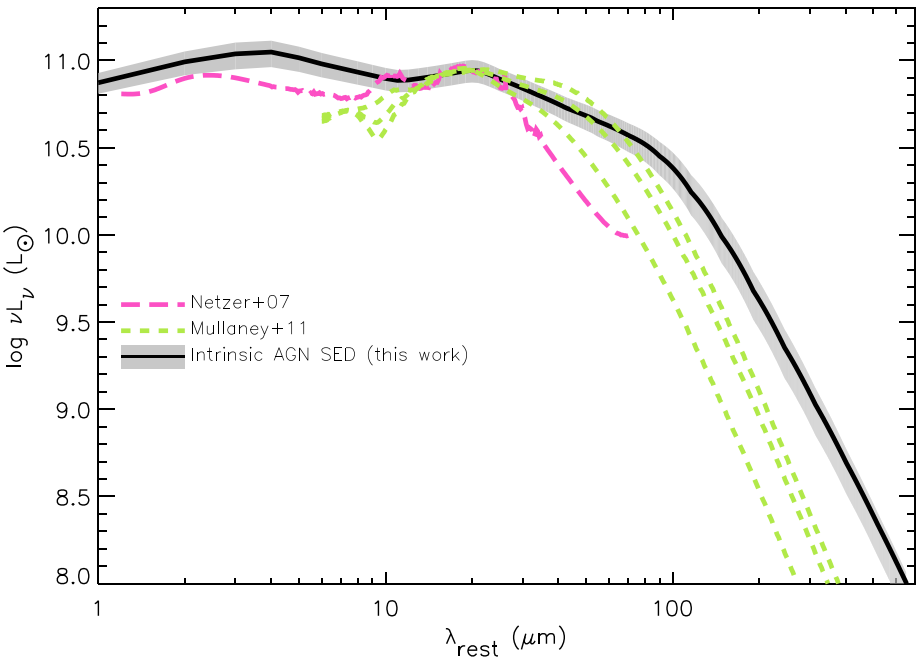

Figure 12. Our intrinsic AGN SED (black solid line) and 68 per cent confidence intervals (shaded region). For comparison, the intrinsic AGN SEDs form Netzer et al. (2007) and Mullaney et al. (2011) are also shown, normalized at 20 μm.

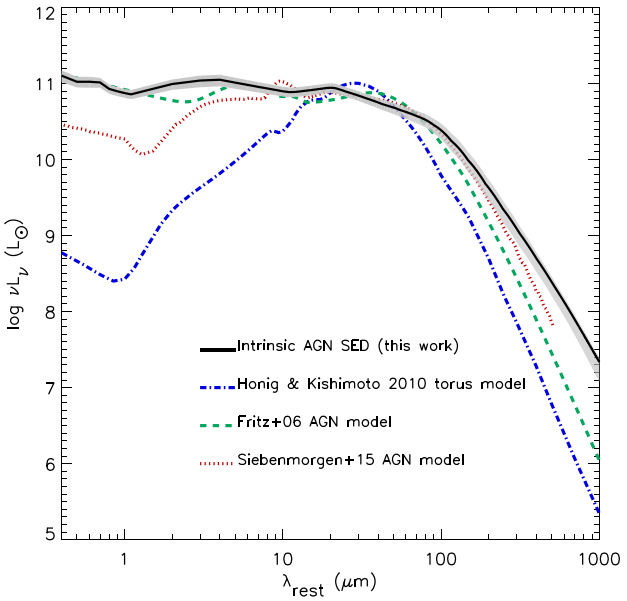

Figure 13. Plot highlighting the differences between the intrinsic AGN SED (this work) and synthetic AGN models. The blue dot–dashed line is the best-fitting torus model from Hönig & Kishimoto (2010), the green dashed line is the best-fitting model from Fritz et al. (2006) and the red dotted line is the best-fitting model from Siebenmorgen, Heymann & Efstathiou (2015).

2006). Netzer et al. produce a template starburst SED by normalizing the SEDs of the starburst-dominated ULIRGs in their sample at 60 μm and then taking the mean at every wavelength. To determine the intrinsic AGN SED, they subtract the starburst template from the average PG QSO SED, first scaling it according to the assumption that most of the 50–100 μm emission from the PG QSOs is due to star formation. Note that our study suggests that this assumption is not valid. Mullaney et al. (2011) estimate the form of an intrinsic AGN SED by decomposing the observed SEDs of the sources in their sample into host-galaxy and intrinsic AGN components by simultaneously fitting the mid-IR spectra and *IRAS* photometry. Their method however already assumes an intrinsic AGN component which is then used during spectral decomposition, created by combining the mid-IR spectra of AGN-dominated sources in the 6–25 μm range with a modified blackbody above a wavelength λ_{BB}, where λ_{BB} is allowed any value between 25 and 100 μm. The drawbacks of both Netzer et al. and Mullaney et al. methods is that they make a priori assumptions about the balance of AGN and stellar emission when calculating the intrinsic AGN SED. In contrast, we argue that our method of extracting the pure AGN emission is more robust as it is not based in any inherent assumptions on the balance of AGN and stellar emission or the shape of the intrinsic AGN component. The intrinsic AGN SED derived here maintains a higher level of far-IR emission compared to the Mullaney et al. and Netzer et al. SEDs. This far-IR excess likely stems from AGN heated dust in the host galaxy (at kpc scales), a component which is not accounted for in the Mullaney et al. and Netzer et al. SEDs.

4.3 Comparison with AGN models

In Fig. 13, we compare our intrinsic AGN SED to torus models from Hönig & Kishimoto (2010, hereafter HK10) and accretion disc+torus models from Fritz et al. (2006, hereafter F06) and Siebenmorgen et al. (2015, hereafter S15). Our aim is to examine whether the aforementioned widely used AGN models could reproduce our pure AGN SED in the far-IR/submm, resulting in the appropriate normalization of an SF far-IR/submm component during multicomponent SED fitting (e.g. see Hatziminaoglou et al. 2008, for multicomponent SED fitting). The HK10 library of torus models is fit on to our pure AGN SED in the 3–100 μm region, whereas the F06 and S15 libraries are fit from 0.4 to 100 μm as they include the accretion disc component. In Fig. 13, we examine how well the best-fitting model (minimum χ^2) from each library can reproduce the far-IR, $\lambda > 100$ μm, emission of our intrinsic AGN SED.

The best-fitting HK10 model has 0 inclination angle (type-I AGN), a 30° half opening angle of the torus, PL index alpha of 0 (the lower alpha is the redder the SED), the highest number of clouds ($N = 10$) which gives maximum IR emission and the highest optical depth $\tau = 80$ increasing the flux at longer wavelengths. From the F06 library, the best-fitting model is for a face-on AGN, has the largest opening angle, no variation of the dust density in the vertical direction, a value of 10 for the equatorial optical depth at 9.7 μm and a ratio of 150 between the outer and inner radius of the dust distribution. The best-fitting S15 model has an inner torus radius of 15.45×10^{17} cm (maximum in the library), a cloud volume filling factor of 1.5 per cent, 0 optical depth in the individual clouds, maximum optical depth in the disc mid-plane (1000), and a viewing angle of 43° measured from the z-axis.

We see that the HK10 and F06 AGN models fail to reproduce the AGN power in the submm, whereas the S15 model does a better job, matching the mid to far-IR part of our SED up to about 200 μm. This shortfall is likely due to the limited extent of the dust distribution in the formulation of these models and hence caution must be applied when using AGN models in SED multicomponent fitting, as it could lead to overestimated SFRs.

4.4 Implications for measuring SFRs in AGN host galaxies

Our work suggests that for AGN hosts, particularly those of powerful AGN, the contribution from the AGN to the infrared/submm needs to be taken into account when calculating properties such as SFRs. In Fig. 14, we use three luminous QSO samples from the literature to demonstrate the level of correction that would be required when measuring the SF emission in luminous AGN. We use type 1 radio-quiet QSOs with robust submm/mm detections at $1.7 < z < 2.9$ from Lutz et al. (2008), 24 μm-selected broad-line QSOs at $1.7 < z < 3.6$ from Dai et al. (2012) and X-ray absorbed and submm luminous type I QSOs at $1.7 < z < 2.8$ from Khan-Ali et al. (2015). The 60 μm luminosity of each source ($\nu L^{tot}_{\nu,60}$) is shown as a function of $\nu L^{AGN}_{\nu,5100}$, using their published values or values obtained by private communication. The shaded region is our pure AGN SED, its width corresponding to the 20 per cent error on the $\nu L_{\nu,60}/\nu L_{\nu,5100}$ ratio calculated by bootstrapping. Using our pure AGN SED, we subtract the expected AGN contribution to $\nu L^{tot}_{\nu,60}$, obtaining the luminosity at 60 μm which can solely be attributed to star formation ($\nu L^{SF}_{\nu,60}$). Note that in many cases $\nu L^{SF}_{\nu,60}$ is up to an order of magnitude lower than $\nu L^{tot}_{\nu,60}$. Fig. 14 illustrates that one could assume a negligible AGN contribution only if the total galaxy emission at 60 μm is more than a factor of 2 higher than the intrinsic AGN power measured in the optical, i.e. $\nu L^{tot}_{\nu,60}/\nu L^{AGN}_{\nu,5100} > 2$. In fact, the AGN contribution cannot be simply ignored even at $\lambda > 200$ μm; the third panel of Fig. 5 shows that in our sample, the average AGN SED is at least comparably luminous to the average SF SED at all wavelengths suggesting that, in some galaxies hosting luminous AGN, there is no 'safe' broad-band photometric observation ($\lesssim$1000 μm) that can be assumed free from AGN

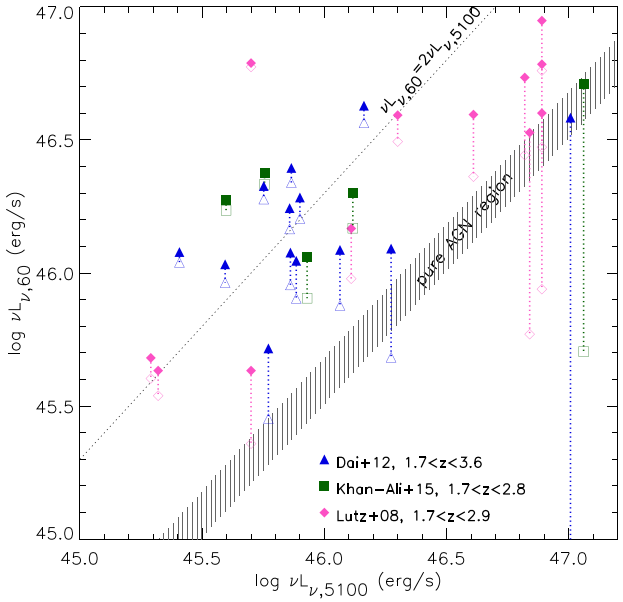

Figure 14. 60 μm luminosity versus AGN power ($\nu L^{\rm AGN}_{\nu,5100}$) for three luminous high-redshift QSO samples from the literature: Dai et al. (2012, $1.7 < z < 3.6$), Khan-Ali et al. (2015, $1.7 < z < 2.8$) and Lutz et al. (2008, $1.7 < z < 2.9$). The grey shaded region is the pure AGN line (±20 per cent uncertainty on the $\nu L_{\nu,60}/\nu L_{\nu,5100}$ ratio calculated by bootstrapping). The filled-in symbols are the 60 μm luminosity of each source ($\nu L^{\rm tot}_{\nu,60}$) whereas the open symbols are the 60 μm luminosity attributed to star formation with the AGN contribution subtracted ($\nu L^{\rm SF}_{\nu,60}$). The dotted line is at $\nu L^{\rm tot}_{\nu,60}/\nu L^{\rm AGN}_{\nu,5100} = 2$ and represents the ratio above which the AGN contribution to the far-IR SED may be ignored.

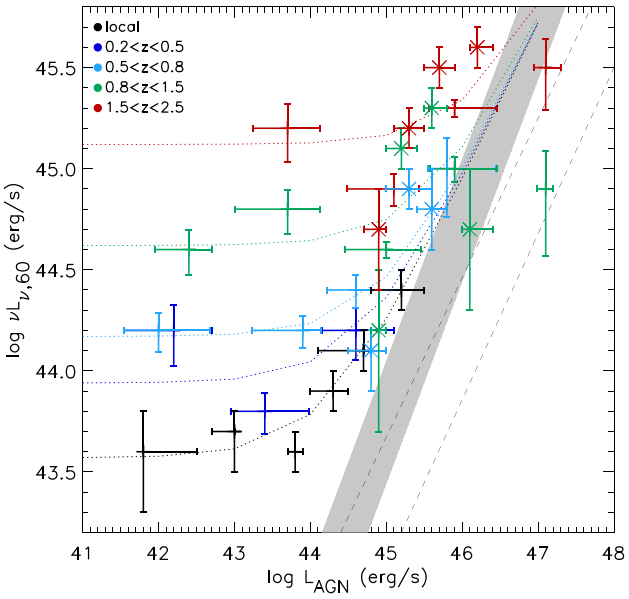

Figure 15. Average 60 μm rest-frame luminosity versus AGN luminosity from Rosario et al. (2012; crosses and dotted lines) and (2013; asterisks). The colours represent different redshift bins as shown in the legend. The region bound by the dashed lines is the Rosario et al. estimate of a pure AGN contribution. The shaded region is the pure AGN region derived in this work, its width incorporating the range in $\nu L_{\nu,5100}$–$L_{\rm AGN}$ conversion factors (see Section 4.4) together with the 20 per cent uncertainty in $\nu L_{\nu,60}/L_{\rm AGN}$ that we calculate from bootstrapping.

contamination. Assuming an M82 SED (from the SWIRE SED library) where $L_{\rm IR,8–1000\,\mu m} = 1.7\nu L_{\nu,\,60}$, broadly speaking, the AGN contribution could be ignored if the total IR emission from a given galaxy is more than a factor of 4 higher than the intrinsic AGN power at 5100 Å.

A further point to note is that submm colours are not necessarily good indicators of whether the galaxy is AGN or SF dominated in the far-IR/submm. Although the pure AGN SED and the SEDs of SFGs are distinctly different at $\lesssim$100 μm, they decay with a similar rate in the submm (e.g. see Fig. 5), as in both cases we are into the Rayleigh–Jeans part of the modified blackbody emission from dust in the host galaxy. As a result, we would expect that all SEDs would have consistent submm colours. Indeed, we find that the rest-frame *Herschel*/SPIRE 500/350 μm and 350/250 μm colours of our pure AGN SED are within the range probed by nearby spiral galaxies (Boselli et al. 2010). Redshifting the AGN SED to $z = 2$, the observed SPIRE colours now coincide with the peak in the observed distribution of colours in SPIRE-selected galaxies and AGN as shown in Hatziminaoglou et al. (2010). This implies that the rest-frame submm colours (or observed submm colours at low redshift) of AGN hosts are not an indication of whether AGN or star formation is the dominant energy source in the submm.

We next examine the implications of our pure AGN SED for the statistical studies of star formation in X-ray selected AGN from Rosario et al. (2012, 2013) and Harrison et al. (2012). Rosario et al. (2012, 2013) examine the SF properties of X-ray selected AGN hosts, using the 60 μm luminosity as a proxy for star formation and assuming a negligible contribution from the AGN at 60 μm; in Fig. 15, we show the average luminosities for the Rosario et al. samples as well as the functional fits to them. Also plotted is the region in parameter space that corresponds to the intrinsic AGN emission in their work, derived by using the AGN SEDs of Mullaney et al. (2011) and Netzer et al. (2007). The shaded region represents the $L_{60}/L_{\rm AGN}$ ratio that stems from our intrinsic AGN SED. As in Rosario et al. (2012, 2013), to convert from $\nu L_{\nu,\,5100}$ to $L_{\rm AGN}$, where $L_{\rm AGN}$ is the bolometric AGN luminosity, we use the Netzer & Trakhtenbrot (2007) relation $L_{\rm AGN} = f \times \nu L_{\nu,\,5100}$, where $f = 7$. However as Netzer & Trakhtenbrot (2007) point out, estimates for f in type 1 AGN are in the range 5–13 (e.g. Elvis et al. 1994; Kaspi, Brandt & Schneider 2000; Netzer 2003; Marconi et al. 2004). The range in $\nu L_{\nu,\,5100}$ to $L_{\rm AGN}$ conversion factors quoted above are incorporated into the width of the intrinsic AGN region together with the 20 per cent uncertainty in $\nu L_{\nu,\,60}/L_{\rm AGN}$ that we calculate from bootstrapping.

Note that our pure AGN SED shifts the $\nu L_{\nu,\,60}/L_{\rm AGN}$ ratio to higher values, i.e. the AGN contribution at 60 μm is now 2–10 times higher than what is assumed in the work of Rosario et al. (2012, 2013). Rosario et al. interpret their results as two different mechanisms at play regarding the black hole/SF connection, originally proposed by Shao et al. (2010); they suggest that for low AGN luminosities, the SFR does not correlate with AGN power, so secular mechanisms drive the black hole and galaxy growth, whereas at high AGN luminosities there is a correlation, a sign of the increasing importance of major-mergers in driving both the growth of supermassive black holes and star formation. Looking at Fig. 15 and the location of the pure AGN region derived in this work, we arrive at a different interpretation of the Rosario et al. results: we propose that the difference in $\nu L_{\nu,\,60}/L_{\rm AGN}$ between the low- and high-luminosity AGN can be understood simply as an increase in the AGN contribution. In Fig. 15, it is evident that one can only travel so far in the x-direction before the pure AGN region (grey shaded region) is met, so for a given level of $\nu L_{\nu,\,60}$, low-luminosity AGN can have

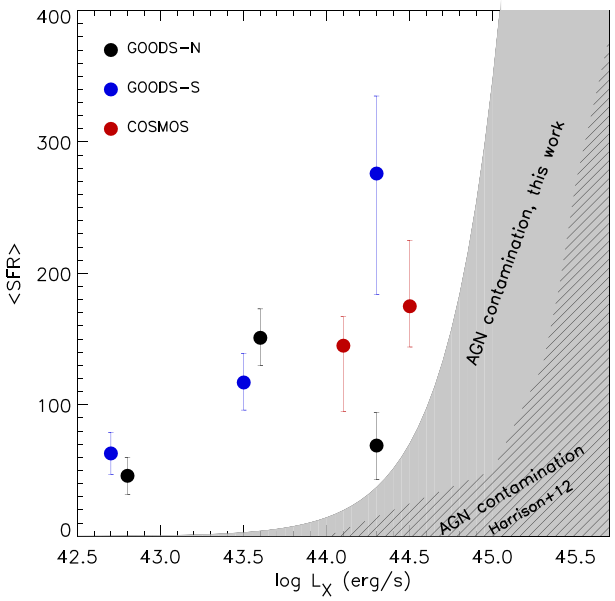

Figure 16. Average SFR versus X-ray AGN luminosity for the X-ray selected sample of AGN at $z = 1$–3 in Harrison et al. (2012). The regions of AGN contamination are also shown – shaded area: this work, hatched area: Harrison et al. (2012)

a higher fraction of star formation contribution than their higher luminosity counterparts. In other words, at any given redshift, and hence mean SFR, the more luminous AGN will on average have higher $\nu L_{\nu,60}$ simply due to increased AGN emission at 60 μm. Our results indicate that the apparent correlation between $\nu L_{\nu,60}$ and $L_{\rm AGN}$ in high-luminosity AGN is driven by the intrinsic AGN emission at those wavebands, also corroborated by the convergence of the $\nu L_{\nu,60}$–$L_{\rm AGN}$ trends (dotted lines) on to the intrinsic AGN region (grey shaded region) at high $L_{\rm AGN}$.

Fig. 16 shows the results from Harrison et al. (2012), who examined the average SFR in a sample of luminous X-ray selected AGN at $z = 1$–3. The SFRs presented are not corrected for AGN contamination and the parameter space assigned to the AGN contribution is shown. Following their method, we also calculate a region of AGN contamination, first using our pure AGN SED to obtain the rest-frame luminosity at 83 μm (250 μm observed at $z = 2$) and then converting it to an SFR using the Elbaz et al. (2011) main-sequence template and the Kennicutt (1998) relation. To convert from $\nu L_{\nu,5100}$ to $L_{\rm X}$, we use the Maiolino et al. (2007) relation, $\log L_{\rm X}(2\text{–}10\,{\rm keV}) = 0.721 \times \log(\nu {\rm L}_{\nu,5100}) + 11.78$, where the units are in erg s^{-1}. The region of AGN contamination derived using our pure AGN SED extends further than the one shown in Harrison et al., implying a correction in the SFRs would be necessary for the most luminous AGN. Indeed correcting for AGN contamination might bring these results in agreement with Page et al. (2012) who find that the most luminous AGN do not lie in the most highly SF hosts (see also Barger et al. 2015).

5 SUMMARY AND CONCLUSIONS

We have explored the question of whether and how much the AGN contributes to the far-IR emission from a galaxy. For our purposes we used a sample of 47 broad line, luminous ($L_{5100} > 10^{43.5}$ erg s^{-1}), $z < 0.18$, radio-quiet QSOs from the Palomar Green survey. Taking advantage of archival data in the 0.4–500 μm range and PAH-derived estimates of SF luminosities, we removed the stellar component in these sources' energy budget using the 11.3 μm PAH feature in the QSOs' mid-IR spectra, in order to obtain an average *intrinsic* or *pure* AGN SED in the optical–submm wavelength range. The 1σ uncertainty on the intrinsic AGN SED ranges between 12 and 45 per cent as a function of wavelength and is a combination of PAH flux measurement errors and the uncertainties related to the conversion between PAH luminosity and SF luminosity.

Our main conclusions are as follows.

(i) In our sample of QSOs, the average AGN contribution to the total energy budget is >95 per cent shortwards of 20 μm, 60–95 per cent in the 20–100 μm range and at all wavelengths thereafter (at least up to 1000 μm) it is comparable to the contribution from star formation. This implies that for some galaxies hosting powerful AGN, the entire optical-submm broad-band SED can be AGN dominated and hence there is no 'safe' waveband (at $\lambda < 1000$ μm) that can be used in calculating SFRs without subtracting the AGN contribution.

(ii) Our intrinsic AGN SED maintains a higher level of far-IR emission compared to other such SEDs available in the literature. This far-IR excess likely stems from AGN heated dust in the host galaxy (at kpc scales), a component which had been previously ignored.

(iii) Using AGN torus models in AGN/SF SED decomposition could potentially underestimate the far-IR contribution of the AGN and lead to overestimated SFRs, as many of these models are built with a limited extent in the dust distribution.

(iv) The shape of the far-IR component of the intrinsic AGN SED does not vary with AGN luminosity and our AGN template can be considered applicable to any samples of galaxies hosting a luminous (L_{5100} or $L_{\rm X(2-10keV)} \gtrsim 10^{43.5}$ erg s^{-1}) AGN.

(v) Statistical studies of star formation in AGN host galaxies need to incorporate a correction for the AGN contribution, irrespective of the waveband used to calculate SFRs. This is particularly crucial for luminous (L_{5100} or $L_{\rm X(2-10keV)} \gtrsim 10^{43.5}$ erg s^{-1}) AGN. For ease, and broadly speaking, the AGN contamination could be neglected if the intrinsic AGN power at 5100 Å is more than a factor of 2 lower than the galaxy's 60 μm luminosity and more than factor of 4 lower than the total IR emission (8–1000 μm) of the galaxy.

ACKNOWLEDGEMENTS

The *Herschel* spacecraft was designed, built, tested, and launched under a contract to ESA managed by the *Herschel*/Planck Project team by an industrial consortium under the overall responsibility of the prime contractor Thales Alenia Space (Cannes), and including Astrium (Friedrichshafen) responsible for the payload module and for system testing at spacecraft level, Thales Alenia Space (Turin) responsible for the service module, and Astrium (Toulouse) responsible for the telescope, with in excess of a hundred subcontractors. PACS has been developed by a consortium of institutes led by MPE (Germany) and including UVIE (Austria); KU Leuven, CSL, IMEC (Belgium); CEA, LAM (France); MPIA (Germany); INAF-IFSI/OAA/OAP/OAT, LENS, SISSA (Italy); IAC (Spain). This development has been supported by the funding agencies BMVIT (Austria), ESA-PRODEX (Belgium), CEA/CNES (France), DLR (Germany), ASI/INAF (Italy), and CICYT/MCYT (Spain). SPIRE has been developed by a consortium of institutes led by Cardiff University (UK) and including Univ. Lethbridge (Canada); NAOC (China); CEA, LAM (France); IFSI, Univ. Padua (Italy); IAC (Spain); Stockholm Observatory (Sweden); Imperial College London, RAL, UCL- MSSL, UKATC, Univ. Sussex (UK);

and Caltech, JPL, NHSC, Univ. Colorado (USA). This development has been supported by national funding agencies: CSA (Canada); NAOC (China); CEA, CNES, CNRS (France); ASI (Italy); MCINN (Spain); SNSB (Sweden); STFC, UKSA (UK); and NASA (USA). HIPE is a joint development (are joint developments) by the *Herschel* Science Ground Segment Consortium, consisting of ESA, the NASA *Herschel* Science Center, and the HIFI, PACS and SPIRE consortia. Funding for SDSS-III has been provided by the Alfred P. Sloan Foundation, the Participating Institutions, the National Science Foundation, and the US Department of Energy Office of Science. The SDSS-III web site is http://www.sdss3.org/. SDSS-III is managed by the Astrophysical Research Consortium for the Participating Institutions of the SDSS-III Collaboration including the University of Arizona, the Brazilian Participation Group, Brookhaven National Laboratory, Carnegie Mellon University, University of Florida, the French Participation Group, the German Participation Group, Harvard University, the Instituto de Astrofisica de Canarias, the Michigan State/Notre Dame/JINA Participation Group, Johns Hopkins University, Lawrence Berkeley National Laboratory, Max Planck Institute for Astrophysics, Max Planck Institute for Extraterrestrial Physics, New Mexico State University, New York University, Ohio State University, Pennsylvania State University, University of Portsmouth, Princeton University, the Spanish Participation Group, University of Tokyo, University of Utah, Vanderbilt University, University of Virginia, University of Washington, and Yale University. This publication makes use of data products from the Two Micron All Sky Survey, which is a joint project of the University of Massachusetts and the Infrared Processing and Analysis Center/California Institute of Technology, funded by the National Aeronautics and Space Administration and the National Science Foundation.

REFERENCES

Ahn C. P. et al., 2012, ApJS, 203, 21
Aitken D. K., Roche P. F., 1985, MNRAS, 213, 777
Allamandola L. J., Tielens A. G. G. M., Barker J. R., 1985, ApJ, 290, L25
Allamandola L. J., Tielens A. G. G. M., Barker J. R., 1989, ApJS, 71, 733
Alonso-Herrero A. et al., 2014, MNRAS, 443, 2766
Azadi M. et al., 2015, ApJ, 806, 187
Baldry I. K., Glazebrook K., Brinkmann J., Ivezić Ž., Lupton R. H., Nichol R. C., Szalay A. S., 2004, ApJ, 600, 681
Barger A. J., Cowie L. L., Owen F. N., Chen C.-C., Hasinger G., Hsu L.-Y., Li Y., 2015, ApJ, 801, 87
Bendo G. J. et al., 2008, MNRAS, 389, 629
Bendo G. J. et al., 2010, A&A, 518, L65
Bendo G. J. et al., 2012, MNRAS, 419, 1833
Bendo G. J. et al., 2013, MNRAS, 433, 3062
Bendo G. J. et al., 2015, MNRAS, 448, 135
Blain A. W., Barnard V. E., Chapman S. C., 2003, MNRAS, 338, 733
Boselli A. et al., 2010, A&A, 518, L61
Boselli A. et al., 2012, A&A, 540, A54
Bower R. G., Benson A. J., Malbon R., Helly J. C., Frenk C. S., Baugh C. M., Cole S., Lacey C. G., 2006, MNRAS, 370, 645
Boyle B. J., Terlevich R. J., 1998, MNRAS, 293, L49
Brandl B. R. et al., 2006, ApJ, 653, 1129
Buchner J. et al., 2014, A&A, 564, A125
Cardamone C. N. et al., 2010, ApJS, 189, 270
Chary R., Elbaz D., 2001, ApJ, 556, 562
Chen C.-T. J. et al., 2013, ApJ, 773, 3
Collinson J. S., Ward M. J., Done C., Landt H., Elvis M., McDowell J. C., 2015, MNRAS, 449, 2174
Croton D. J. et al., 2006, MNRAS, 365, 11
Dai Y. S. et al., 2012, ApJ, 753, 33
Dale D. A., Helou G., 2002, ApJ, 576, 159 (DH02)
Dale D. A., Helou G., Contursi A., Silbermann N. A., Kolhatkar S., 2001, ApJ, 549, 215
Desert F.-X., Boulanger F., Puget J. L., 1990, A&A, 237, 215
Diamond-Stanic A. M., Rieke G. H., 2010, ApJ, 724, 140
Dunne L., Eales S., Edmunds M., Ivison R., Alexander P., Clements D. L., 2000, MNRAS, 315, 115
Dwelly T., Page M. J., 2006, MNRAS, 372, 1755
Elbaz D. et al., 2011, A&A, 533, A119
Elvis M. et al., 1994, ApJS, 95, 1
Engelbracht C. W., Rieke G. H., Gordon K. D., Smith J.-D. T., Werner M. W., Moustakas J., Willmer C. N. A., Vanzi L., 2008, ApJ, 678, 804
Esquej P. et al., 2014, ApJ, 780, 86
Ferrarese L., Merritt D., 2000, ApJ, 539, L9
Förster Schreiber N. M., Roussel H., Sauvage M., Charmandaris V., 2004, A&A, 419, 501
Fritz J., Franceschini A., Hatziminaoglou E., 2006, MNRAS, 366, 767 (F06)
Georgakakis A. et al., 2008, MNRAS, 385, 2049
Gordon K. D., Engelbracht C. W., Rieke G. H., Misselt K. A., Smith J.-D. T., Kennicutt R. C., Jr, 2008, ApJ, 682, 336
Granato G. L., De Zotti G., Silva L., Bressan A., Danese L., 2004, ApJ, 600, 580
Griffin M. J. et al., 2010, A&A, 518, L3
Grupe D., Komossa S., Leighly K. M., Page K. L., 2010; ApJS, 187, 64
Haas M., Müller S. A. H., Chini R., Meisenheimer K., Klaas U., Lemke D., Kreysa E., Camenzind M., 2000, A&A, 354, 453
Haas M. et al., 2003, A&A, 402, 87
Hanami H. et al., 2012, PASJ, 64, 70
Harrison C. M. et al., 2012, ApJ, 760, L15
Hatziminaoglou E. et al., 2008, MNRAS, 386, 1252
Hatziminaoglou E. et al., 2010, A&A, 518L, 33
Hernán-Caballero A. et al., 2009, MNRAS, 395, 1695
Hickox R. C., Mullaney J. R., Alexander D. M., Chen C.-T. J., Civano F. M., Goulding A. D., Hainline K. N., 2014, ApJ, 782, 9
Ho L. C., Keto E., 2007, ApJ, 658, 314
Hönig S. F., Kishimoto M., 2010, A&A, 523, A27 (HK10)
Hunt L. K., Thuan T. X., Izotov Y. I., Sauvage M., 2010, ApJ, 712, 164
Isaak K. G., Priddey R. S., McMahon R. G., Omont A., Peroux C., Sharp R. G., Withington S., 2002, MNRAS, 329, 149
Kaspi S., Brandt W. N., Schneider D. P., 2000, AJ, 119, 2031
Kellermann K. I., Sramek R., Schmidt M., Shaffer D. B., Green R., 1989, AJ, 98, 1195
Kennicutt R. C., Jr, 1998, ARA&A, 36, 189
Kennicutt R. C., Jr, et al., 2009, ApJ, 703, 1672
Khan-Ali A., Carrera F. J., Page M. J., Stevens J. A., Mateos S., Symeonidis M., Orjales J. M. C., 2015, MNRAS, 448, 75
Lagos C. D. P., Padilla N. D., Strauss M. A., Cora S. A., Hao L., 2011, MNRAS, 414, 2148
LaMassa S. M., Heckman T. M., Ptak A., Schiminovich D., O'Dowd M., Bertincourt B., 2012, ApJ, 758, 1
Laor A., 1990, MNRAS, 246, 369
Laurent O., Mirabel I. F., Charmandaris V., Gallais P., Sauvage M., Vigroux L., Cesarsky C., 1999, Ap&SS, 269, 357
Leipski C. et al., 2014, ApJ, 785, 154
Li A., Draine B. T., 2002, ApJ, 572, 232
Lutz D., Sturm E., Genzel R., Spoon H. W. W., Moorwood A. F. M., Netzer H., Sternberg A., 2003, A&A, 409, 867
Lutz D. et al., 2008, ApJ, 684, 853
Magorrian J. et al., 1998, AJ, 115, 2285
Mainieri V. et al., 2011, A&A, 535, A80
Maiolino R., Shemmer O., Imanishi M., Netzer H., Oliva E., Lutz D., Sturm E., 2007, A&A, 468, 979
Maiolino R., Rieke G. H., 1995, ApJ, 454, 95
Marcillac D., Elbaz D., Chary R. R., Dickinson M., Galliano F., Morrison G., 2006, A&A, 451, 57
Marconi A., Risaliti G., Gilli R., Hunt L. K., Maiolino R., Salvati M., 2004, MNRAS, 351, 169

Mullaney J. R., Alexander D. M., Goulding A. D., Hickox R. C., 2011, MNRAS, 414, 1082
Netzer H., 2003, ApJ, 583, L5
Netzer H., Trakhtenbrot B., 2007, ApJ, 654, 754
Netzer H. et al., 2007, ApJ, 666, 806
O'Dowd M. J. et al., 2009, ApJ, 705, 885
Ott S., 2010, in Mizumoto Y., Morita K.-I., Ohishi M., eds, ASP Conf. Ser. Vol. 434, Astronomical Data Analysis Software and Systems XIX. Astron. Soc. Pac., San Francisco, p. 139
Page M. J. et al., 2012, Nature, 485, 213
Pearson C. et al., 2014, Exp. Astron., 37, 175
Peeters E., Spoon H. W. W., Tielens A. G. G. M., 2004, ApJ, 613, 986
Pereira-Santaella M., Alonso-Herrero A., Rieke G. H., Colina L., Díaz-Santos T., Smith J.-D. T., Pérez-González P. G., Engelbracht C. W., 2010, ApJS, 188, 447
Petric A. O., Ho L. C., Flagey N. J. M., Scoville N. Z., 2015, ApJS, 219, 22
Pilbratt G. L. et al., 2010, A&A, 518, L1
Podigachoski P. et al., 2015, A&A, 575, A80
Poglitsch A. et al., 2010, A&A, 518, L2
Polletta M. d. C. et al., 2006, ApJ, 642, 673
Polletta M. et al., 2007, ApJ, 663, 81
Pope A. et al., 2008, ApJ, 675, 1171
Priddey R. S., Isaak K. G., McMahon R. G., Omont A., 2003a, MNRAS, 339, 1183
Priddey R. S., Isaak K. G., McMahon R. G., Robson E. I., Pearson C. P., 2003b, MNRAS, 344, L74
Rafferty D. A., Brandt W. N., Alexander D. M., Xue Y. Q., Bauer F. E., Lehmer B. D., Luo B., Papovich C., 2011, ApJ, 742, 3
Ramos-Almeida C. et al., 2014, MNRAS, 445, 1130
Rawlings J. I. et al., 2013, MNRAS, 429, 744
Richards G. T. et al., 2006, ApJS, 166, 470
Rieke G. H., Alonso-Herrero A., Weiner B. J., Pérez-González P. G., Blaylock M., Donley J. L., Marcillac D., 2009, ApJ, 692, 556
Risaliti G., Maiolino R., Salvati M., 1999, ApJ, 522, 157
Risaliti G. et al., 2006, MNRAS, 365, 303
Roche P. F., Aitken D. K., 1985, MNRAS, 213, 789
Roche P. F., Aitken D. K., Smith C. H., Ward M. J., 1991, MNRAS, 248, 606
Rosario D. J. et al., 2012, A&A, 545, 45
Rosario D. J. et al., 2013, A&A, 560, A72
Roussel H., Sauvage M., Vigroux L., Bosma A., 2001, A&A, 372, 427
Rovilos E. et al., 2012, A&A, 546, A58
Sanders D. B., Phinney E. S., Neugebauer G., Soifer B. T., Matthews K., 1989, ApJ, 347, 29
Savage R. S., Oliver S., 2007, ApJ, 661, 1339
Schawinski K., Virani S., Simmons B., Urry C. M., Treister E., Kaviraj S., Kushkuley B., 2009, ApJ, 692, L19
Schmidt M., Green R. F., 1983, ApJ, 269, 352
Schulze A., Wisotzki L., Husemann B., 2009, A&A, 507, 781
Schweitzer M. et al., 2006, ApJ, 649, 79
Shang Z. et al., 2011, ApJS, 196, 2
Shao L. et al., 2010, A&A, 518, L26
Shi Y. et al., 2006, ApJ, 653, 127
Shi Y. et al., 2007, ApJ, 669, 841
Shi Y., Rieke G. H., Ogle P. M., Su K. Y. L., Balog Z., 2014, ApJS, 214, 23
Shipley H. V., Papovich C., Rieke G. H., Dey A., Jannuzi B. T., Moustakas J., Weiner B., 2013, ApJ, 769, 75
Siebenmorgen R., Krügel E., Spoon H. W. W., 2004, A&A, 414, 123
Siebenmorgen R., Haas M., Krügel E., Schulz B., 2005, A&A, 436, L5
Siebenmorgen R., Heymann F., Efstathiou A., 2015 A&A, 583, 120 (S15)
Silverman J. D. et al., 2009, ApJ, 696, 396
Skrutskie M. F. et al., 2006, AJ, 131, 1163
Smith J. D. T. et al., 2007, ApJ, 656, 770
Smith A. J. et al., 2012, MNRAS, 419, 377
Springel V., Di Matteo T., Hernquist L., 2005, MNRAS, 361, 776
Stanley F., Harrison C. M., Alexander D. M., Swinbank A. M., Aird J. A., Del Moro A., Hickox R. C., Mullaney J. R., 2015, MNRAS, 453, 591
Stierwalt S. et al., 2014, ApJ, 790, 124
Strateva I. et al., 2001, AJ, 122, 1861
Sturm E., Lutz D., Tran D., Feuchtgruber H., Genzel R., Kunze D., Moorwood A. F. M., Thornley M. D., 2000, A&A, 358, 481
Sturm E. et al., 2005, ApJ, 629, L21
Symeonidis M. et al., 2013a, MNRAS, 431, 2317
Symeonidis M. et al., 2013b, MNRAS, 433, 1015
Treyer M. et al., 2010, ApJ, 719, 1191
U V. et al., 2012, ApJS, 203, 9
Veilleux S. et al., 2009, ApJS, 182, 628
Voit G. M., 1992, MNRAS, 258, 841
Watabe Y., Kawakatu N., Imanishi M., 2008, ApJ, 677, 895
Westoby P. B., Mundell C. G., Baldry I. K., 2007, MNRAS, 382, 1541
Younger J. D. et al., 2009, MNRAS, 394, 1685

SUPPORTING INFORMATION

Additional Supporting Information may be found in the online version of this article:

Table D1. Intrinsic AGN SED including the 68 per cent confidence upper and lower bounds (http://www.mnras.oxfordjournals.org/lookup/suppl/doi:10.1093/mnras/stw667/-/DC1).

Please note: Oxford University Press is not responsible for the content or functionality of any supporting materials supplied by the authors. Any queries (other than missing material) should be directed to the corresponding author for this article.

APPENDIX A: QSO SEDs

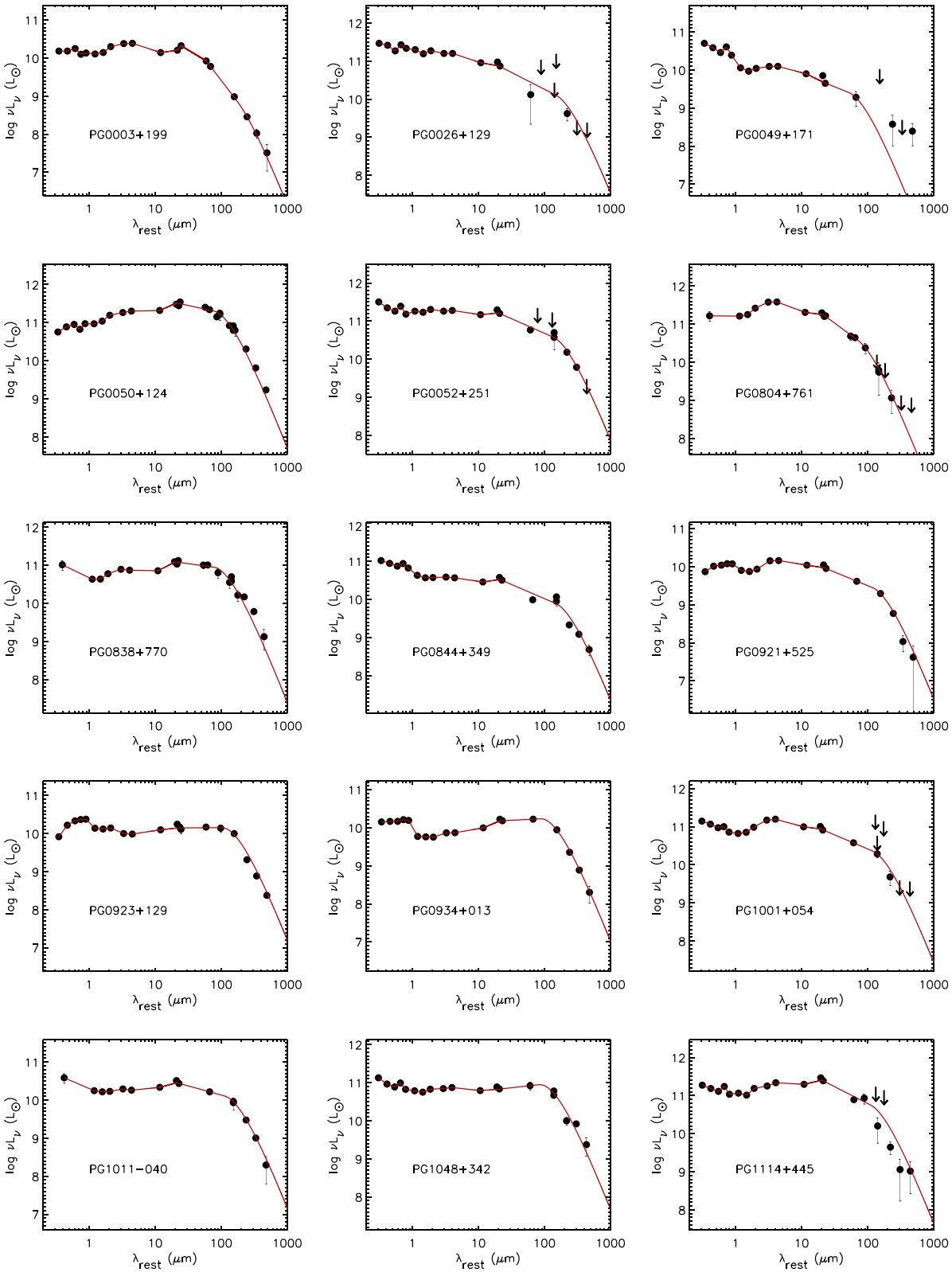

Figure A1. The rest-frame SED of each QSO in our final sample. Photometry is denoted with black filled in circles if $>3\sigma$ and downward arrows if upper limits, and our fit to the data (see Section 3.1) is shown as a red curve.

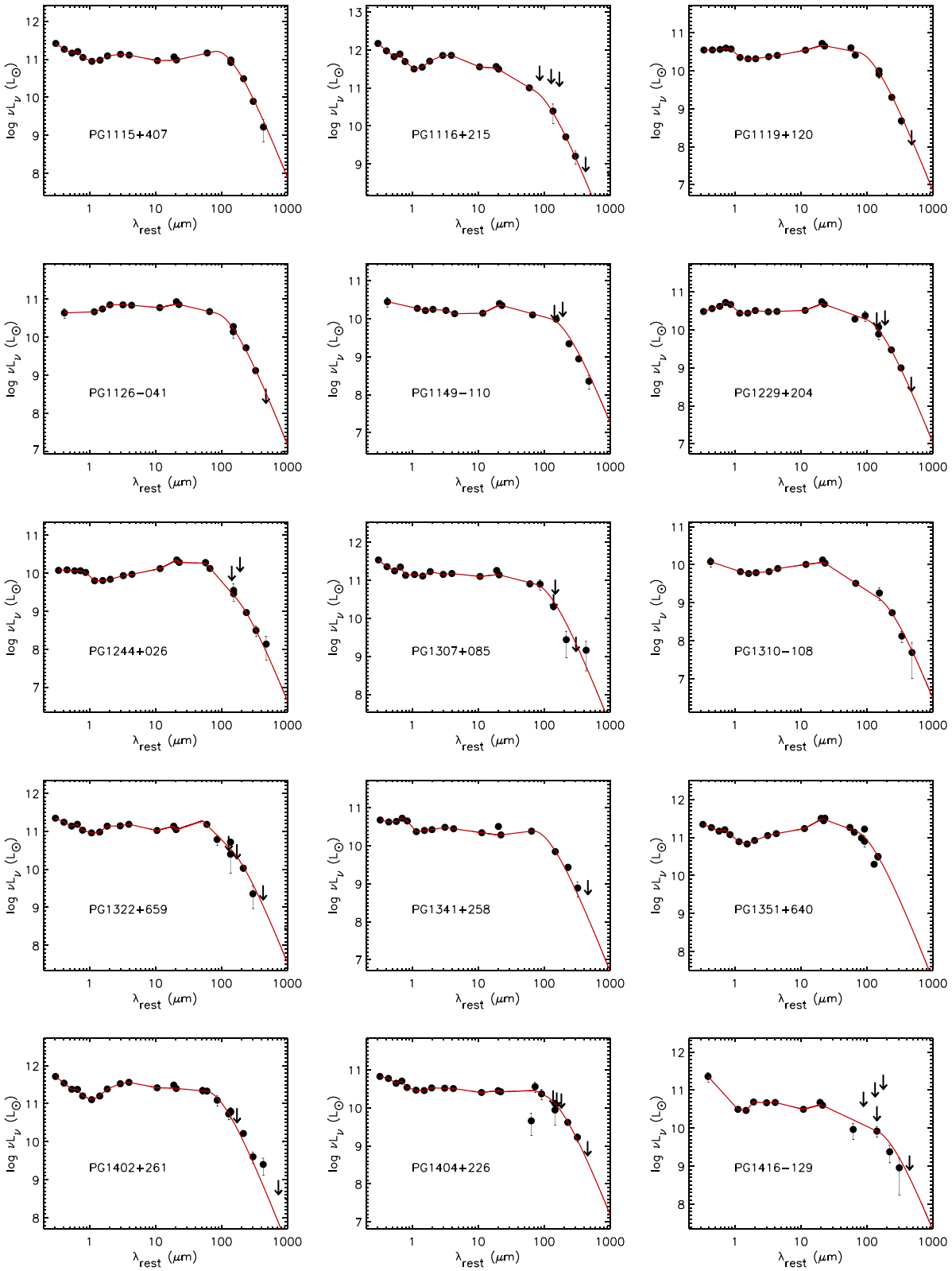

Figure A2. The rest-frame SED of each QSO in our final sample. Photometry is denoted with black filled in circles if $>3\sigma$ and downward arrows if upper limits, and our fit to the data (see Section 3.1) is shown as a red curve.

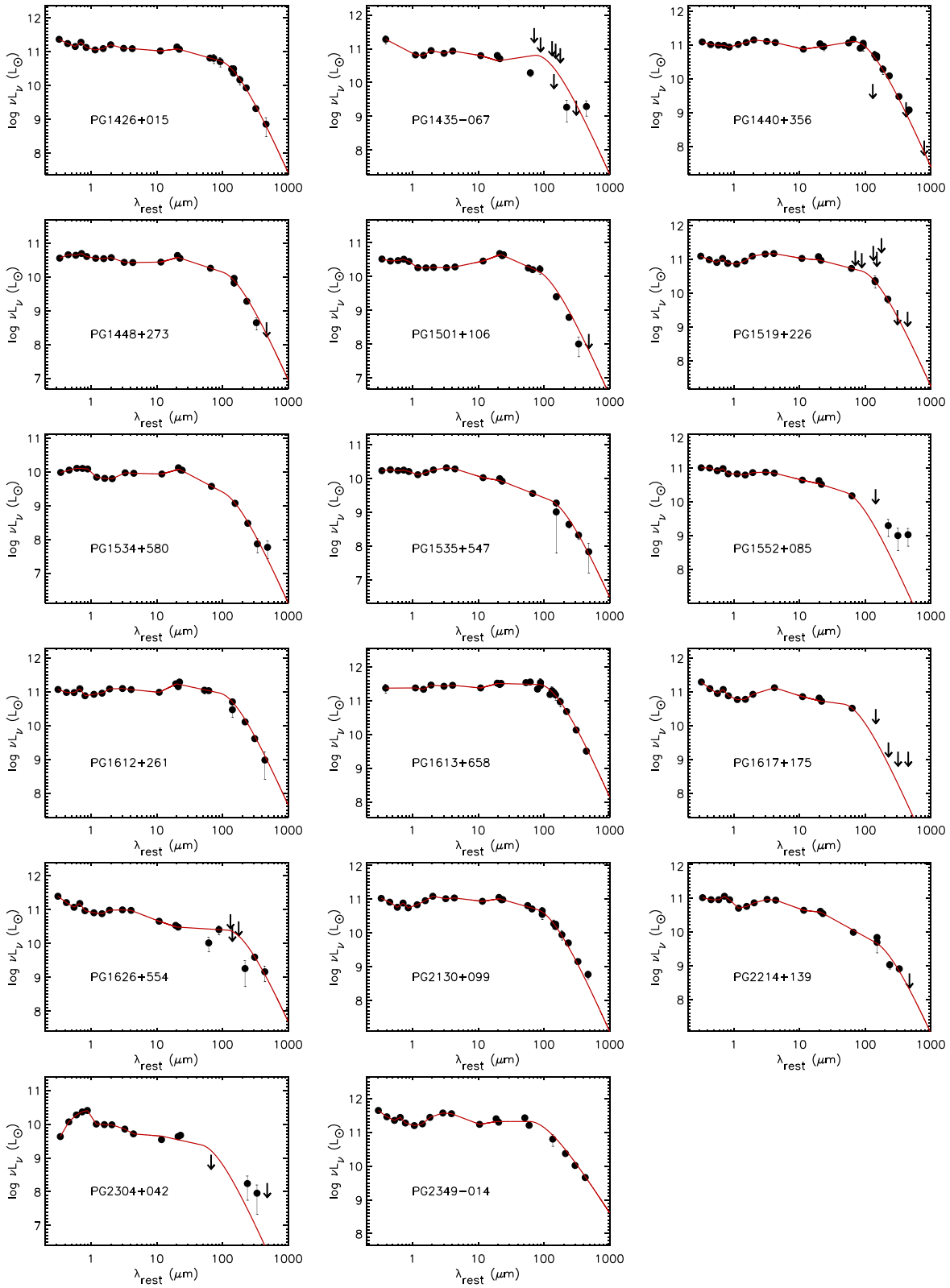

Figure A3. The rest-frame SED of each QSO in our final sample. Photometry is denoted with black filled in circles if $>3\sigma$ and downward arrows if upper limits, and our fit to the data (see Section 3.1) is shown as a red curve.

APPENDIX B: SPIRE DATA

Table B1. SPIRE flux densities and corresponding 1σ uncertainty (in mJy).

Name	f_{250}	σ_{250}	f_{350}	σ_{350}	f_{500}	σ_{500}
PG0003+199	64.01	9.77	33.14	8.57	14.52	9.71
PG0007+106	160.55	8.49	168.07	7.77	150.99	9.87
PG0026+129	24.77	8.90	0.00	7.72	0.00	9.56
PG0049+171	12.16	8.89	0.00	7.42	16.01	9.36
PG0050+124	724.67	11.80	322.41	8.65	121.57	9.58
PG0052+251	73.89	8.92	41.93	7.40	2.55	8.91
PG0157+001	497.43	12.46	180.65	8.22	66.38	9.82
PG0804+761	14.61	8.86	1.54	7.45	0.00	9.87
PG0838+770	103.76	9.00	59.91	7.84	18.70	10.19
PG0844+349	68.59	9.64	54.56	7.68	30.84	9.61
PG0921+525	66.49	8.39	17.02	7.83	9.41	9.29
PG0923+201	3.09	8.76	0.65	7.81	14.94	9.41
PG0923+129	340.31	9.52	178.35	8.25	78.63	9.55
PG0934+013	121.91	9.08	58.27	7.55	21.64	10.18
PG1001+054	21.85	8.77	1.92	7.65	5.33	9.35
PG1011−040	118.77	8.57	56.09	7.53	15.61	10.57
PG1012+008	49.64	8.74	18.32	7.58	0.00	9.96
PG1022+519	127.28	9.66	46.67	7.51	32.21	10.14
PG1048+342	41.24	9.01	47.84	7.49	19.49	9.93
PG1114+445	25.69	9.26	9.28	7.90	12.12	9.01
PG1115+407	152.57	8.91	53.99	7.23	16.32	9.68
PG1116+215	19.09	3.69	8.27	3.14	0.00	3.78
PG1119+120	108.01	8.75	36.23	7.63	1.13	9.48
PG1126−041	195.00	9.31	68.28	7.56	4.05	9.65
PG1149−110	122.67	9.72	68.75	8.06	25.44	9.82
PG1151+117	9.25	9.11	0.14	8.24	0.00	10.02
PG1202+281	36.75	9.08	18.15	7.43	15.60	9.47
PG1211+143	11.46	9.05	5.57	7.22	18.79	9.79
PG1226+023	455.31	6.52	692.08	7.78	1025.31	10.52
PG1229+204	99.07	9.22	46.38	7.77	9.32	9.87
PG1244+026	54.49	8.38	25.85	7.72	16.14	10.12
PG1307+085	13.40	8.96	0.21	7.40	14.14	10.09
PG1309+355	76.71	9.43	37.04	7.30	40.05	9.89
PG1310−108	65.23	8.61	22.21	7.26	11.75	9.27
PG1322+659	43.94	8.52	12.99	7.66	0.00	10.40
PG1341+258	45.67	8.93	18.23	7.83	10.20	10.72
PG1351+236	208.28	9.30	75.56	7.53	13.74	9.29
PG1351+640	0.00	0.00	0.00	0.00	0.00	0.00
PG1352+183	8.73	9.29	1.91	7.66	0.84	10.18
PG1402+261	70.79	8.46	24.21	7.59	21.69	10.18
PG1404+226	54.39	8.74	30.88	7.79	3.99	10.37
PG1415+451	67.04	8.48	27.69	7.90	0.00	9.80
PG1416−129	17.30	8.39	9.20	7.42	0.00	9.28
PG1426+015	146.11	12.13	49.94	9.70	24.64	13.89
PG1435−067	14.25	8.94	4.02	9.13	29.97	14.35
PG1440+356	251.84	8.67	86.19	7.49	49.24	9.27
PG1448+273	59.39	9.75	19.30	7.31	1.81	8.92
PG1501+106	66.20	8.69	15.08	8.74	1.86	13.69
PG1519+226	42.05	9.33	4.48	7.87	0.00	11.99
PG1534+580	49.69	8.14	17.17	7.72	19.34	10.31
PG1535+547	42.04	8.90	28.18	7.41	12.99	9.94
PG1552+085	16.97	8.84	12.04	7.75	18.23	9.84
PG1612+261	91.51	8.90	40.95	7.36	13.59	9.92
PG1613+658	346.13	10.36	137.77	8.00	46.72	9.07
PG1617+175	5.97	8.54	0.00	7.84	3.32	10.09
PG1626+554	12.32	8.71	37.58	7.32	19.76	9.71
PG2130+099	173.01	8.51	68.23	7.28	40.54	10.24
PG2209+184	117.03	9.06	81.58	7.57	74.22	10.09
PG2214+139	33.01	8.25	35.28	7.40	8.41	9.51
PG2304+042	13.51	9.16	9.81	7.46	0.00	9.36
PG2349−014	88.42	3.75	54.83	3.09	34.49	3.93

APPENDIX C: TESTING THE METHOD OF SFR ESTIMATION ON STARBURST GALAXIES

As explained in Section 2.1, we take the value of $L_{\rm SFIR}$ for each QSO from Shi et al. (2007). Shi et al. measure the strength of the 7.7 and 11.3 μm PAHs in the QSO spectra and derive the conversion factor between PAH flux and 8–1000 μm total infrared luminosity attributed to star formation ($L_{\rm SFIR}$) for each PG QSO, by adopting an SED template from the Dale & Helou (2002) library that gives the closest PAH flux at the redshift of the object. Here, we test this method on some samples of nearby starburst galaxies using the 11.3 μm PAH, which is the feature used in deriving $L_{\rm SFIR}$ for the vast majority of our sample.

(i) Following the method of Shi et al. (2007), we assign total infrared luminosities ($L_{\rm IR}$; 8–1000 μm) to the DH02 SED library using the 60/100 μm colour and the relation in Marcillac et al. (2006), $\log(f_{60}/f_{100}) = 0.128 \log L_{\rm IR} - 1.611$. Each SED template is subsequently normalized to units of $L_\odot$ by its $L_{\rm IR}$.

(ii) We measure the luminosity of the 11.3 PAH (*single feature*) in each DH02 template by integrating under the feature in the 10.9–11.8 μm region and subtracting the continuum in the same region (the continuum baseline estimated by interpolating between 10.9 and 11.8 μm). We also measure the luminosity of the PAH 11.3 *complex* (as in Stierwalt et al. 2014) by integrating in the 10.9–13.1 μm wavelength range.

(iii) For the first comparison we use starburst galaxies from Brandl et al. (2006) and Pereira-Santaella et al. (2010), 28 sources in total (we refer to this as sample A). We take the 11.3 μm single feature PAH luminosities published in these papers and *IRAS* far-IR fluxes from NASA Extragalactic Database (NED), the latter simply converted to rest-frame luminosities, with no *K*-corrections required as these are nearby galaxies. For the second comparison, we use 31 starburst galaxies from GOALS (we refer to this as sample B) which have published *Spitzer*/MIPS fluxes in U et al. (2012) and 11.3 complex PAH fluxes in Stierwalt et al. (2014). Again these are nearby galaxies so no *K*-corrections are necessary. Note that all galaxies are larger than the *Spitzer*/IRS slit, so we correct the published PAH luminosities according to the factors tabulated in these papers.

(iv) Each starburst galaxy is then assigned the DH02 template which has the closest PAH luminosity to the true PAH luminosity of the source (single feature for sample A, complex feature for sample B). We then average the templates matched to sample A and B separately and compare with the average true far-IR SEDs built using the *IRAS* and *Spitzer* photometry. The 1σ uncertainties are calculated by bootstrapping the matched SED templates for each sample. The results are shown in Figs C1 and C2. There is excellent agreement between the true *Spitzer* or *IRAS*-derived SEDs and the average SEDs derived using our method from the PAH measurements.

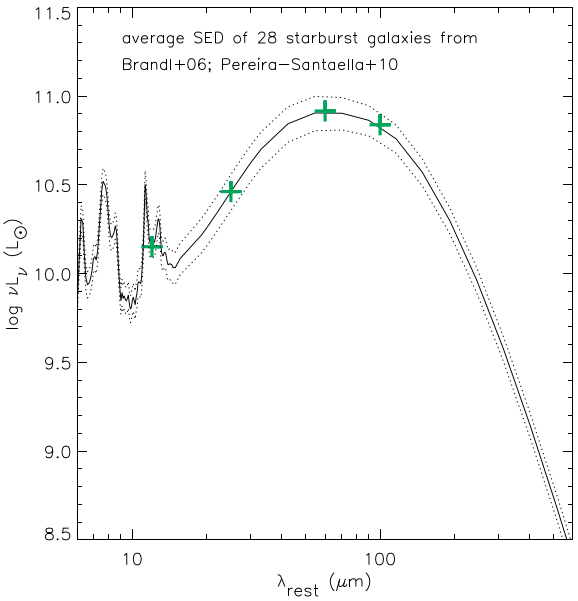

Figure C1. The average template SED of sample A (28 sources; Brandl et al. 2006; Pereira-Santaella et al. 2010; solid curve and dotted curves for the 1σ uncertainty calculated by bootstrapping) compared with the true average luminosities of this sample from *IRAS* photometry at 12, 25, 60 and 100 μm (green crosses). There is excellent agreement between the true *IRAS*-derived average SED and the average SED derived using our method from the PAH measurements.

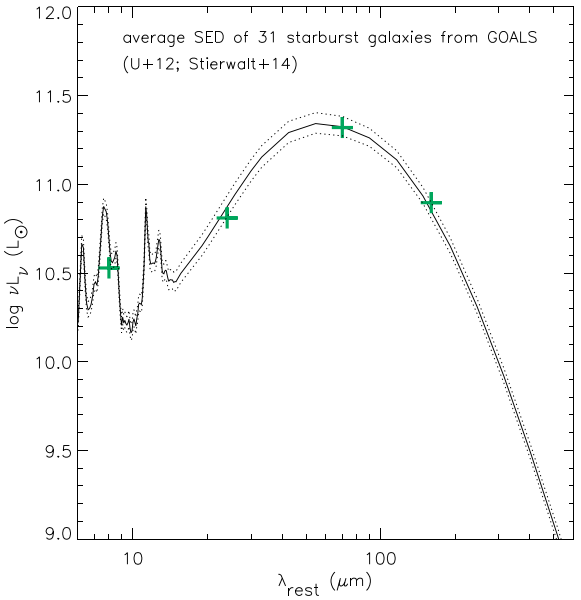

Figure C2. The average template SED of sample B (31 sources; U et al. 2012; Stierwalt al. 2014; solid curve and dotted curves for the 1σ uncertainty calculated by bootstrapping), compared with the true average luminosities of this sample from *Spitzer* photometry at 8, 24, 70 and 160 μm (green crosses). There is excellent agreement between the true *Spitzer*-derived average SED and the average SED derived using our method from the PAH measurements.

APPENDIX D: THE INTRINSIC AGN SED

Table D1. Intrinsic AGN SED including the 68 per cent confidence upper and lower bounds. This table can be found in the online version of the journal, only the first few entries are shown here.

$\lambda_{\rm rest}$ μm	log [νL_ν] $L_\odot$	log [$\nu L_{\nu,\rm upper}$] $L_\odot$	log [$\nu L_{\nu,\rm lower}$] $L_\odot$
0.4	11.10	11.17	11.02
0.5	11.02	11.09	10.95
0.6	11.02	11.09	10.94
0.7	11.01	11.07	10.94
0.8	10.93	10.98	10.86
0.9	10.90	10.95	10.83
1	10.87	10.93	10.81
2	10.99	11.05	10.92
3	11.04	11.10	10.95
4	11.05	11.11	10.96
5	11.02	11.08	10.93
6	10.98	11.04	10.90
7	10.96	11.02	10.88
8	10.93	11.00	10.86
9	10.91	10.98	10.84
10	10.90	10.96	10.83

This paper has been typeset from a TEX/LATEX file prepared by the author.